

# Thesis Title

by

E. Ross



A thesis submitted to the  
University of Birmingham  
for the degree of  
DOCTOR OF PHILOSOPHY

Solar and Stellar Physics Group (SASP)  
School of Physics and Astronomy  
University of Birmingham  
Birmingham, B15 2TT  
Month 20XX

# Contents

<b>List of Figures</b>	<b>vi</b>
<b>List of Tables</b>	<b>vii</b>
<b>List of Abbreviations</b>	<b>ix</b>
<b>1 Introduction</b>	<b>1</b>
1.1 Introduction . . . . .	1
1.2 Space Weather . . . . .	1
1.2.1 Forbush Decreases . . . . .	1
1.2.2 Ground Level Enhancements . . . . .	2
1.3 Cosmic Rays . . . . .	2
1.3.1 . . . . .	2
1.4 The HiSPARC Experiment . . . . .	2
1.4.1 HiSPARC Project . . . . .	2
1.4.2 HiSPARC Detector and Station Configuration . . . . .	2
1.5 The Solar Mean Magnetic Field . . . . .	8
1.5.1 . . . . .	8
<b>2 HiSPARC as a Space Weather Detector</b>	<b>9</b>
2.1 Introduction . . . . .	9
2.2 Aims . . . . .	12
2.3 HiSPARC Data . . . . .	13
2.4 Station Properties . . . . .	15
2.4.1 Cut-Off Rigidity . . . . .	15
2.4.2 Asymptotic Viewing Directions . . . . .	19
2.5 HiSPARC Observations . . . . .	20
2.5.1 Observations of Ground Level Enhancements . . . . .	20
2.5.2 Observations of Forbush Decreases . . . . .	23
2.6 Atmospheric Corrections of HiSPARC Data . . . . .	26
2.6.1 Motivation . . . . .	26
2.6.2 Barometric Correction . . . . .	26
2.6.3 Temperature Correction . . . . .	29
2.7 HiSPARC Observations After Atmospheric Corrections . . . . .	31
2.7.1 Observations of Ground Level Enhancements . . . . .	31
2.7.2 Observations of Forbush Decreases . . . . .	33
2.8 Air Shower Simulations . . . . .	35

2.8.1	Motivation . . . . .	35
2.8.2	Air Shower Footprints . . . . .	35
2.8.3	Muon Flux . . . . .	37
2.8.4	Muon Flux From MAIRE . . . . .	40
2.9	Conclusion . . . . .	44
	<b>Bibliography</b>	<b>48</b>

# List of Figures

1.1	Schematic diagram of the HiSPARC scintillation detector. (A): PMT; (B): light-guide adaptor; (C): light-guide; (D): scintillator. . . . .	3
1.2	Typical formations of two-detector and four-detector stations. In each, the grey circle denotes a GPS antenna which is located in between the detectors to provide a precise timestamp for each signal. . . . .	5
1.3	(a): An example PMT signal after digital conversion by the HiSPARC electronics box. The horizontal lines denote: the noise cut-off (dotted line), which is used for setting a limit when integrating the pulse height, to give the pulse integral; the low-voltage threshold (dash-dot); the high-voltage threshold (dashed). (b) The pulse height distribution over the course of a single day from HiSPARC station 501. The vertical lines show the low-voltage threshold (dash-dot) and the high-voltage threshold (dashed). . . . .	7
2.1	GLEs observed by the NM stations based at Oulu. Top panel: GLE 70; middle panel: GLE 71, bottom panel: GLE 72. The solid-black line shows the 2-minute-averaged, pressure corrected data and the vertical, dashed-red lines show the epochs of each GLE onset. The units of time on the x-axis are, MM-DD HH. . . . .	11
2.2	FDs observed by the NM stations based at Oulu. Top left panel: FDs during March 2012; top right panel: FD during July 2012; bottom left panel: FD during December 2014; bottom right panel: FD during September 2017. The solid-black line shows the 2-minute-averaged, pressure corrected data and the vertical, dashed-blue lines show the epochs of each FD onset. The units of time on the x-axis are, YYYY-MM-DD. . . . .	12
2.3	The geographic location of each HiSPARC station considered in this work. Each green circle denotes the location of a detector station. . . . .	15
2.4	The availability of data for each HiSPARC station considered, for each of the space weather epochs listed in Table 2.1. The purple grids denote no available data, teal denotes that only the events data are available, and yellow denotes that both the events and singles data are available. . . . .	16
2.5	Azimuthal and zenith angle variations in the allowed and forbidden rigidity trajectories for HiSPARC station 501. The forbidden trajectories are in black. . . . .	18

2.6	The vertical asymptotic viewing directions of 5 HiSPARC stations. The rigidity range of the simulations were from $1.0 \text{ GV} < R < 20.0 \text{ GV}$ , and the results are plotted in geographic coordinates on January 20th 2005. The diamonds correspond to the HS ground location and the circles correspond to the AVD for a specific rigidity value. . . . .	19
2.7	HiSPARC data for stations 501 and 3001 around the epoch of GLE 70 on 13/12/2006. The plot shows the minute-averaged and 5-minute-averaged trigger events between detectors within the station. The vertical red, dashed line depicts the approximate onset time of the GLE. The units of time on the x-axis are, MM-DD HH. . . . .	21
2.8	HiSPARC data for stations 8001 and 3001 around the epoch of GLE 71 on 17/05/2012. The plot shows the minute-averaged and 5-minute-averaged trigger events between detectors within the station. The vertical red, dashed line depicts the approximate onset time of the GLE. The units of time on the x-axis are, MM-DD HH. . . . .	21
2.9	HiSPARC data for 4 stations around the epoch of GLE 72 on 10/09/2017. The top panel of each subplot shows the minute-averaged trigger events between detectors within the station, while the bottom panel shows the mean-shifted, minute-averaged counts by each individual detector in the station. The vertical red, dashed line depicts the approximate onset time of the GLE. The units of time on the x-axis are, MM-DD HH. . . . .	22
2.10	HiSPARC data for stations 501 and 8001 around the epoch of the FDs in March 2012. The plot shows the minute-averaged and hourly-averaged trigger events between detectors within the station. The vertical blue-dashed lines show the approximate onset-time of the FDs. The units of time on the x-axis are, YYYY-MM-DD. . . . .	23
2.11	HiSPARC data for stations 501 and 8001 around the epoch of the FD in July 2012. The plot shows the minute-averaged and hourly-averaged trigger events between detectors within the station. The vertical blue-dashed line shows the approximate onset-time of the FD. The units of time on the x-axis are, YYYY-MM-DD. . . . .	23
2.12	HiSPARC data for four stations around the epoch of the FD in December 2014. The plot shows the minute-averaged and hourly-averaged trigger events between detectors within the station. The vertical blue-dashed line shows the approximate onset-time of the FD. The units of time on the x-axis are, YYYY-MM-DD. . . . .	24

2.13	HiSPARC data for four stations around the epoch in which there were two FDs close to the onset of GLE 72. The top panel of each subplot shows the minute-averaged trigger events between detectors within the station, while the bottom panel shows the mean-shifted, minute-averaged counts by each individual detector in the station. The vertical blue-dashed lines show the approximate onset-times of the two FDs observed around this epoch and the red-dashed line depicts the approximate onset time of the GLE. The units of time on the x-axis are, YYYY-MM-DD. . . . .	25
2.14	The anti-correlation between CR count rates and the atmospheric pressure. (a) shows the CR and the local atmospheric pressure measured at a NM in the South Pole; (b) shows the CR and pressure measured by HiSPARC station 501. . . . .	27
2.15	The barometric coefficient calculation: (a) during November 2017 for the South Pole (SOPO) NM station, (b) during November 2019 for HiSPARC station 501 at Nikhef. . . . .	28
2.16	A comparison between the monthly barometric coefficient computed in this work and using the online barometric coefficient tool throughout the year 2017 for the SOPO NM station. . . . .	29
2.17	.....	31
2.18	Atmospheric-corrected HiSPARC data for 2 stations around the epoch of GLE 71. The top panel of each subplot shows the minute-averaged trigger events between detectors within the station, while the bottom panel shows the mean-shifted, minute-averaged counts by each individual detector in the station. The vertical red, dashed line depicts the approximate onset time of the GLE. . . . .	32
2.19	Full atmospheric-corrected HiSPARC data for 2 stations around the epoch of GLE 72. The top panel of each subplot shows the minute-averaged trigger events between detectors within the station, while the bottom panel shows the mean-shifted, minute-averaged counts by each individual detector in the station. The vertical red, dashed line depicts the approximate onset time of the GLE. . . . .	32
2.20	Full atmospheric correction of HS 8001 (Eindhoven) data during... .	33
2.21	HS 501 (Nikhef) . . . . .	33
2.22	Pressure corrected HiSPARC data for 2 stations in an epoch where there were two FDs close to the onset of GLE 72. The top panel of each subplot shows the minute-averaged events data, while the bottom panels show the mean-shifted, minute-averaged counts by each individual detector in the stations. The vertical blue-dashed lines show the approximate onset-times of the FDs and the red-dashed line depicts the approximate onset-time of the GLE. . . . .	34
2.23	Mean muon density footprints for (a) proton-initiated air showers and (b) $\alpha$ -particle-initiated air showers with initial PCR trajectories with zenith angles $\theta = 0^\circ$ and various PCR energies. The error bars given represent $1\sigma$ . . . . .	36

2.24	Mean number of muons produced at ground level by the PCR for (a) proton-initiated air showers and (b) $\alpha$ -particle-initiated air showers, for various PCR energy. . . . .	38
2.25	.....	39
2.26	Plots of the calculated MAIRE muon spectra for different incident spectra. Blue and orange lines show muon spectra calculated for the incident GCR spectra during solar minimum and maximum, respectively. The other coloured lines show the computed muon spectra for the incident GLE spectra. (a) shows the individual muon spectra for GCRs and GLEs; (b) shows the combined muon spectra for the GCR at solar maximum and the GLEs. . . . .	41

# List of Tables

2.1	Largest space weather events since the beginning of HiSPARC, which will be searched for within the HiSPARC data. The percentage change column provides a reference of how much the CR counts observed by the NM station at Oulu ( $R_c=0.81$ GV) and Kiel ( $R_c=2.36$ GV) increased or decreased by, due to the space weather event. More precise times for the event onset can be found at <a href="#">NMDB (2018)</a> (for GLEs) and <a href="#">Lingri et al. (2016)</a> (for FDs). . . . .	10
2.2	Properties of some of the HiSPARC stations: geographic longitude ( $\phi$ ), geographic latitude ( $\lambda$ ), altitude ( $h$ ), and the geomagnetic vertical cut-off rigidity ( $R_C$ ) calculated from the PLANETOCOSMICS simulations. . . . .	18
2.3	The seven GLEs where MAIRE muon spectra were available, and the maximum observed increase in the neutron flux in the NMDB and the station where the increase was observed. . . . .	40
2.4	Observed and predicted increases in the CR count rates at the Kiel NM station. The observed neutron increases use data from the NMDB, where the errors are the measurement uncertainty from the 5-minute averaged data. The predicted data for the neutrons and muons are from the MAIRE simulations. The ratio column provides a conversion factor from the MAIRE predicted neutron increases compared to those observed. . . . .	42
2.5	The MAIRE predicted increase in the muon flux, adjusted for the calibration factor between observed and predicted neutron increases at the Kiel station, in Table 2.4. . . . .	43

# List of Abbreviations

**AMS-02** Alpha Magnetic Spectrometer.

**AVD** Asymptotic Viewing Direction.

**CORSIKA** Cosmic Ray Simulations for Kascade.

**CR** Cosmic Ray.

**EAS** Extensive Air Shower.

**ESD** Event Summary Data.

**FD** Forbush Decrease.

**GCR** Galactic Cosmic Ray.

**GLE** Ground Level Enhancement.

**GPS** Global Positioning System.

**HiSPARC** High School Project on Astrophysics and Research with Cosmics.

**IGRF** International Geomagnetic Reference Field.

**ISS** International Space Station.

**MAIRE** Model for Atmospheric Ionising Radiation Effects.

**MD** Muon Detector.

**MIP** Minimum Ionising Particle.

**MPV** Most Probable Value.

**NM** Neutron Monitor.

**NMDB** Neutron Monitor Data Base.

**PCR** Primary Cosmic Ray.

**PMMA** Polymethylmethacrylate.

**PMT** Photo Multiplier Tube.

**SAPPHiRE** Simulation and Analysis Program Package for HiSPARC Research and Education.

**SCR** Solar Cosmic Ray.

**SEP** Solar Energetic Particle.

**UHECR** Ultra-High Energy Cosmic Ray.

# 1 Introduction

*While the majority of this chapter was written for the thesis, parts of Sec ?? were written for ? and have been adapted from the introduction in that work to limit repetition. **YOU WANT SOMETHING LIKE THIS AT THE START OF EACH SCIENCE CHAPTER TOO, TO SHOW WHAT YOU DID AND ANY ACKNOWLEDGEMENTS OF OTHER PEOPLE***

## 1.1 Introduction

...

In this thesis we ...

Before we start on the main body of the thesis, the contents of each chapter and the main themes within are given in outline first.

Chapter ...

Chapter ...

Chapter ...

In Chapter ...

In Chapter ... Finally the thesis is concluded in Chapter ...

## 1.2 Space Weather

### 1.2.1 Forbush Decreases

...

## 1.2.2 Ground Level Enhancements

...

## 1.3 Cosmic Rays

### 1.3.1 ...

...

## 1.4 The HiSPARC Experiment

### 1.4.1 HiSPARC Project

HiSPARC stands for *High School Project on Astrophysics and Research with Cosmics*, and it is a scientific outreach project that was initiated in the Netherlands in 2002 (Bartels, 2012). The HiSPARC project has two main goals: the study of Ultra-High Energy Cosmic Ray (UHECR) for astroparticle physics research, and to serve as a resource to expose high school students to scientific research (Bartels, 2012).

HiSPARC is a global network of muon detectors spread across the Netherlands, Denmark, the UK, and Namibia. The detectors at each station record muon counts and may be used for many scientific experiments, such as: reconstruction of the direction of a cosmic ray induced air shower, reconstruction of the energy of the air shower's primary particle, investigation between the atmospheric conditions and the number of cosmics rays observed, etc.

Data recorded by the HiSPARC stations are stored and are available publicly at <http://www.hisparc.nl>, where the Cosmic Ray (CR) counts, atmospheric data, station metadata, and more can be found.

### 1.4.2 HiSPARC Detector and Station Configuration

The detection philosophy of HiSPARC is to sample the footprints of Extensive Air Showers (EASs) using coincident triggers between scintillation detectors. As Hi-

PARC was set up as an outreach programme for high schools, this impacted detector design. Resources are limited in schools and the detectors are usually financed by the participating high schools, colleges, and universities. In addition, students (accompanied by their teachers and local node support staff) are responsible for assembly and installation their detectors, which are typically installed on the roofs of schools. Due to this, the detectors needed to be cheap, robust, and easily maintainable, therefore the scintillation detector was selected for the HiSPARC network.

Scintillators consist of materials that emit light when charged particles pass through them with sufficient energy to ionise the scintillator material. The total light produced is proportional to the number of charged particles, and can be collected by a Photo Multiplier Tube (PMT). Each HiSPARC detector utilises a plastic scintillator of dimensions 1000 mm x 500 mm x 20 mm, providing a detection area of 0.5 m<sup>2</sup>. A vertically incident Minimum Ionising Particle (MIP) has a most probable energy loss in 2 cm of the scintillation material of 3.51 MeV ( $\equiv 1$  MIP) ([van Dam et al., 2020](#)).

The scintillator is glued to a triangular/‘fish-tailed’ light-guide (dimensions, base: 500 mm; top: 25 mm; height: 675 mm), and a light-guide adapter provides the optical interface between the square end of the light-guide and the cylindrical aperture of the PMT. The configuration of a single HiSPARC detector is shown in Figure 1.1.

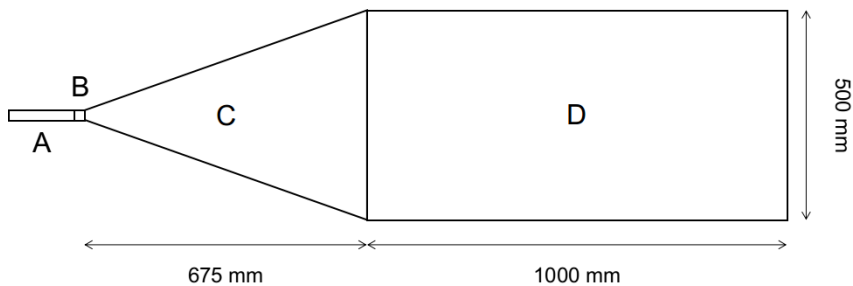


Figure 1.1: Schematic diagram of the HiSPARC scintillation detector. (A): PMT; (B): light-guide adaptor; (C): light-guide; (D): scintillator.

The scintillator is made of a material consisting of polyvinyltoluene as the base, with anthracene as the fluor, and the emission spectrum peaks at a wavelength of

425 nm (Fokkema, 2012; Bartels, 2012). The light-guide is made from Polymethylmethacrylate (PMMA) and has a comparable refractive index to the scintillator (1.58 and 1.49, respectively), reducing refraction effects between the two materials (van Dam et al., 2020).

The PMT used is an ETEEnterprises 9125B PMT, with a 25 mm aperture, blue-green sensitive bialkali photocathode, and 11 high-gain dynodes (Bartels, 2012; ETEEnterprises, 2020). The quantum efficiency of the PMT used in the HiSPARC detectors peaks at around 375 nm at 28%, and at 425 nm the quantum efficiency is 25% (Fokkema, 2012).

Each detector is wrapped in aluminium foil (thickness 30  $\mu\text{m}$ ) and a black, vinyl material (thickness 0.45 mm), which is usually used as a pond liner, to ensure light-tight detectors and to reduce the noise level from stray photons (van Dam et al., 2020). In addition, each detector is placed inside of its own a plastic roof box to again ensure that it is light-tight, and to also ensure that it is weather-proof, as the detectors are usually located on the roofs of schools, colleges, and universities.

A HiSPARC station combines either 2 or 4 detectors, to observe coincident muons ('events'), and typical configurations of each are shown in Figure 1.2. The separation between detectors varies from station-to-station. In addition some stations have the capability to measure the local atmospheric properties, such as temperature, pressure, relative humidity etc. Moreover, some stations also record the 'singles' rates, i.e. the frequency at which an individual detector is triggered, independently of the other detectors in the station. The singles rates are important when investigating non-EAS events.

light pulse which is converted into an electric pulse by the PMT. This pulse is sampled and digitized at 400 MHz

The PMTs of the detector in a station are connected to HiSPARC electronics boxes, which sample and digitise the signal at a rate of 400 MH, and each PMTs is connected to the electronics box using cables of a standard length of 30 m, to



(a) Two-detector station configuration



(b) Four-detector station configuration (triangle arrangement)



(c) Four-detector station configuration (diamond arrangement)

Figure 1.2: Typical formations of two-detector and four-detector stations. In each, the grey circle denotes a GPS antenna which is located in between the detectors to provide a precise timestamp for each signal.

minimise any timing offsets between detectors ([Fokkema, 2012](#); [van Dam et al., 2020](#)). The electronics boxes are capable of controlling and reading two PMTs, therefore a four-detector station requires two electronics boxes: a master and a

slave.

The HiSPARC experiment is set up in such a way as to ensure that each station across the HiSPARC network reads a similar count rate of muons, in order to aid the direct comparison between the different stations in the network. When configuring the station, a trigger threshold must be applied for the PMT signals. This is standardised across the HiSPARC network and can be seen in relation to a detector trigger pulse in Figure 1.3a. There are two thresholds, low: 30 mV, which represents 0.2 of a MIP; high: 70 mV, which represents 0.5 of a MIP ([Fokkema, 2012](#); [van Dam et al., 2020](#)). The thresholds were chosen to increase the sensitivity of the stations for observing gamma rays and low energy electrons, but this has the effect of making it more difficult to determine whether an individual detection is from a muon, or another MIP. This is why the HiSPARC network usually relies on detecting ‘events’, from coincident muons.

Each detector in the network is set up such that the pulseheight spectrum peaks at a Most Probable Value (MPV) of  $\sim 150$  mV (see Figure 1.3), and such that the high threshold allows a mean count rate on the order 100 counts per second and the low threshold allows a mean count rate of the order 400 counts per second; these can be tuned by adjusting the PMT voltage. It could be argued that in setting up the detectors in this way, there is an immediate bias in the data to reject lower energy CRs.

The pulse height spectrum (see Figure 1.3b) is composed of two main regions: the left side which falls off rather steeply and the main, asymmetric part of the spectrum which features a peak and a long tail. The left side of the spectrum is understood to be from high-energy photons (gamma rays) produced in air showers ([Fokkema, 2012](#)). These high-energy photons may undergo pair production when interacting with the scintillator which may produce ionising electron and positron pairs. The trigger thresholds are placed to reject these noise signals from the data.

The main, asymmetric distribution which features a peak and a tail is from

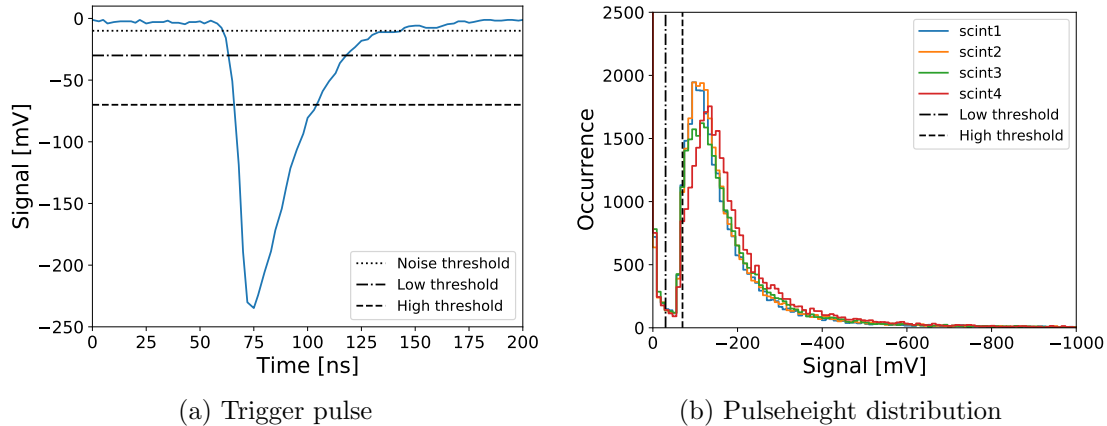


Figure 1.3: (a): An example PMT signal after digital conversion by the HiSPARC electronics box. The horizontal lines denote: the noise cut-off (dotted line), which is used for setting a limit when integrating the pulse height, to give the pulse integral; the low-voltage threshold (dash-dot); the high-voltage threshold (dashed). (b) The pulse height distribution over the course of a single day from HiSPARC station 501. The vertical lines show the low-voltage threshold (dash-dot) and the high-voltage threshold (dashed).

charged particles (muons and electrons) ([van Dam et al., 2020](#)). The mean energy loss of particles in a material is described by the Blethe-Bloch formula; however this does not account for fluctuations in energy loss ([Fokkema, 2012](#)). A Landau distribution in fact describes the fluctuations in energy loss of particles. Due to the resolution of the HiSPARC detectors the distribution in Figure 1.3b is best described by the convolution of the Landau distribution with a normal distribution which describes the resolution of the detector ([Fokkema, 2012](#)). The peak of the distribution, the most probable values (MPV), is the most likely energy lost by a particle in the detector, i.e. the 3.51 MeV MIP ([van Dam et al., 2020](#)). It has been shown that the location of the MPV can vary due to the effects of atmospheric temperature ([Bartels, 2012](#); [van Dam et al., 2020](#)).

The default trigger conditions for detecting an air shower event between multiple PMTs within a station differ for a two/four-detector station. In a two-detector station, an event is recorded if the PMT signals from both detectors exceed the low threshold within the coincidence time window ( $1.5\ \mu\text{s}$ ). In a four-detector station, there are two conditions: (i) at least two detectors exceed the high threshold within

the coincidence time window; (ii) at least three detectors exceed the low threshold within the coincidence time window. These are the default conditions, but there are other, user configurable ways of triggering the station.

The scientific goals that can be achieved also vary between the two/four-detector stations. When at least three detectors in a four-detector station observe particles of an EAS, the direction of the EAS (and thus the direction of the Primary Cosmic Ray (PCR)) can be acquired using triangulation calculations. When only two detectors in a station observe particles of an EAS, i.e. the limit for a two-detector station, it is only possible to reconstruct the arrival direction along the axis that connects the centres of those two detectors (thus it is not possible to reconstruct the direction of the PCR).

## 1.5 The Solar Mean Magnetic Field

### 1.5.1 ...

...

## 2 HiSPARC as a Space Weather Detector

### 2.1 Introduction

[Space weather events have been regularly monitored by Cosmic Rays (CRs) detector since... CITE!...]

[comment on the SEPs causing space weather events and refer to papers which state earlier arrival times of higher energy SEPs, i.e. those which will be monitored by muon detectors, cite to: <https://iopscience.iop.org/article/10.1088/0004-637X/761/2/101> / and from here: <https://academic.oup.com/pasj/article/68/1/8/2469980>, we get the quote: "The different behaviours observed between the muon detector and the NMs can be linked with the different particle species observed by these two detectors. The muon component of the cosmic rays is known as the hard component due to their large penetration. Thus, the signal at muon detectors can be linked with the maximum flare energy release during the impulsive phase of the flare (duration no longer than 20min)."]

[From Lingri et al. (2016): "The majority of Forbush Decreases (FDs) are produced by CMEs with velocities from 400 to 1200 km/sec and at the same time the velocity of the solar wind fluctuates from 400 to 740 km/sec"]

[The High School Project on Astrophysics and Research with Cosmics (HiSPARC) was initiated in 2005 (CITE!!!)...]

HiSPARC was set up with the detection philosophy of observing Extensive Air Shower (EAS), which are typically associated with Primary Cosmic Rays (PCRs) with energy of  $\sim 10^{14}$  eV and above, that produce large footprints observable with

Table 2.1: Largest space weather events since the beginning of HiSPARC, which will be searched for within the HiSPARC data. The percentage change column provides a reference of how much the CR counts observed by the NM station at Oulu ( $R_c=0.81$  GV) and Kiel ( $R_c=2.36$  GV) increased or decreased by, due to the space weather event. More precise times for the event onset can be found at [NMDB \(2018\)](#) (for GLEs) and [Lingri et al. \(2016\)](#) (for FDs).

GLE Onset	GLE	% Change		FD Onset	% Change	
		Oulu	Kiel		Oulu	Kiel
13/12/2006	70	~ 90%	~ 30%	08/03/2012	~ 10%	~ 10%
17/05/2012	71	~ 15%	~ 3%	12/03/2012	~ 3 – 5%	~ 3 – 5%
10/09/2017	72	~ 5%	N/A	14/07/2012	~ 3 – 5%	~ 5 – 10%
				21/12/2014	~ 5 – 10%	~ 5 – 10%
				06/09/2017	~ 1 – 2%	N/A
				07/09/2017	~ 6%	N/A

many HiSPARC stations simultaneously. For PCRs with energy below  $\sim 10^{14}$  eV the air shower is small, with almost no observable muon footprint, and for PCRs with energy below  $\sim 10^{11}$  eV, there is typically fewer than one or two muons that reach the ground, making their observation difficult. Most muons produced by such low-energy PCRs decay higher in the atmosphere and their energy is mostly transferred into the resultant electron ([van Dam et al., 2020](#)), which is observable by HiSPARC.

The HiSPARC detectors are capable of observing any muons that reach them, therefore the project was motivated by the existing network of Muon Detector (MD) which may have the capability of observing the CRs associated with space weather events.

[Pull together a discussion here on the existing published literature using hisparc data...]

[In this work, we provide a study to investigate whether the existing HiSPARC network is capable of observing space weather events. break down the sections...??]

Few space weather events have been observed over the lifetime of the HiSPARC network; however, Table 2.1 outlines the specific space weather driven Ground Level Enhancements (GLEs) and FDs that occurred since the beginning of HiSPARC that will be investigated in this work.

The specific events in Table 2.1 were selected as: (i) for the GLEs, they are the only three that fall in the HiSPARC operational period; (ii) for the FDs, they are the only individual, or set of, FDs that result in a count variation in excess of  $\sim 5\%$  and the largest FDs are likely to be the most promising candidates for observation with HiSPARC.

For comparison with the HiSPARC results, we show the GLEs, as observed by the Oulu Neutron Monitor (NM) station, in Figure 2.1. It is clear from Figure 2.1 that the relative increase of the GLE was large for GLEs 70 and 71, but much more subtle for GLE 72. We expect that if we are to observe any of the GLEs, we shall have the best chance of observing GLE 70. Similarly, we show a comparison plot for the FDs, as observed by the Oulu NM station, in Figure 2.2. Each FD produces a moderate decrease in the NM count rate.

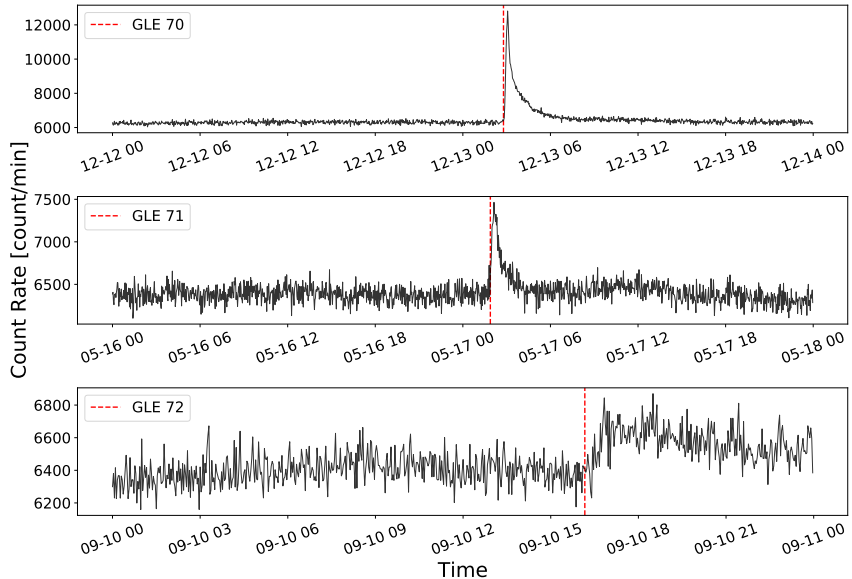


Figure 2.1: GLEs observed by the NM stations based at Oulu. Top panel: GLE 70; middle panel: GLE 71, bottom panel: GLE 72. The solid-black line shows the 2-minute-averaged, pressure corrected data and the vertical, dashed-red lines show the epochs of each GLE onset. The units of time on the x-axis are, MM-DD HH.

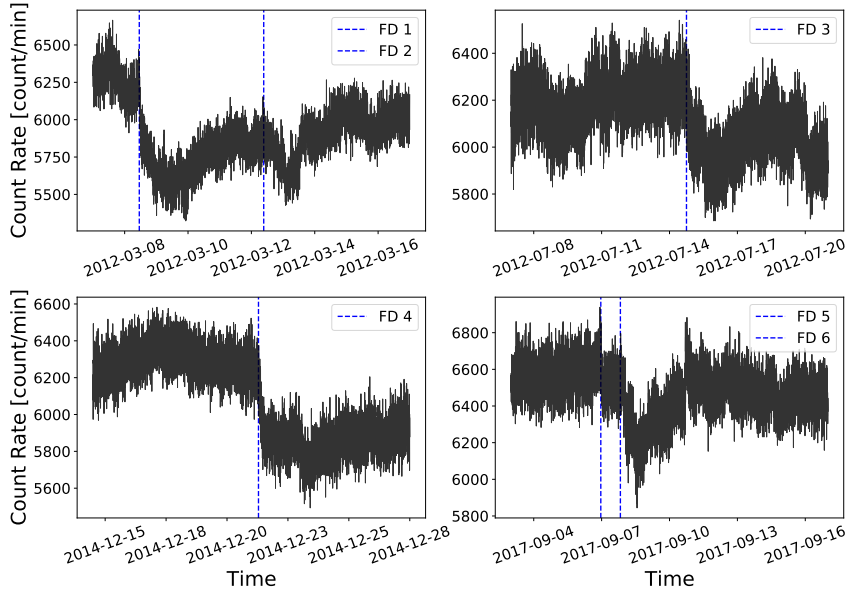


Figure 2.2: FDs observed by the NM stations based at Oulu. Top left panel: FDs during March 2012; top right panel: FD during July 2012; bottom left panel: FD during December 2014; bottom right panel: FD during September 2017. The solid-black line shows the 2-minute-averaged, pressure corrected data and the vertical, dashed-blue lines show the epochs of each FD onset. The units of time on the x-axis are, YYYY-MM-DD.

## 2.2 Aims

The principle aim of the project was to determine whether the existing HiSPARC network is capable of observing space weather events. To do this, we investigated the properties of the HiSPARC detectors, to learn about what typical PCRs we observe. This was initially achieved by investigating the data during periods of space weather activity to search for the associated signatures. We searched through some of the most reliable HiSPARC stations to determine whether these events were observed in the data. This was done to determine whether, without much effort, we could get a binary answer on whether these events were observed by HiSPARC.

Following this, we performed simulations of air showers initiated by CRs to understand the expected muon flux and dispersion at ground level. This helped us to understand how likely it is to observe the PCRs associated with space weather with the HiSPARC detectors, observing muons.

Finally, ground-based observations of muons from air showers are susceptible

to the conditions in the atmosphere; therefore, where possible, we corrected for atmospheric effects and again reviewed the corrected data to determine whether the space weather events were observed.

## 2.3 HiSPARC Data

The HiSPARC cosmic ray data are available on the HiSPARC Public Database<sup>1</sup>. There each station is listed and they are all grouped by their local nodes. For every station one can see its ID, name, and a coloured square and circle displaying its current data delivery and data acquisition status, respectively. Clicking on any station takes you to a dedicated page which displays its data on a user-selected day. Here it is possible to download the events data, singles data, and weather data, where available. It is also possible to download coincidence data between multiple stations, where different stations measure the same event; it is possible to determine if stations measured the same event by comparing the Global Positioning System (GPS) timestamps of events. The data are stored in `HDF5` format, but are downloaded in `.tsv` format.

This method of obtaining HiSPARC data is acceptable if only a small quantity of data are needed, but it is cumbersome if large quantities of data are required. To obtain large quantities of HiSPARC data, it was more efficient to use the Event Summary Data (ESD) module within the Simulation and Analysis Program Package for HiSPARC Research and Education (SAPPHiRE) Python package ([Fokkema et al., 2012](#)). The data are downloaded in the raw `HDF5` format, and can then be manipulated using further Python scripts.

A Python script was written, which used the SAPPHiRE ESD module, to request the download, from a user-specified station, of a specific type of data (i.e. events, singles, weather), download and open the `HDF5` table, manipulate the data to either keep them in the raw cadence, or resample into other timebases, and finally store the

---

<sup>1</sup><https://data.hisparc.nl/>

data in .csv format. This reduced the complexity involved in downloading the data and provided a repeatable method of acquiring the HiSPARC data in a consistent format.

There exists some  $\sim 140$  stations in the HiSPARC network (van Dam et al., 2020) which have been uploading data for varying durations since the beginning of the project in 2005. It was too challenging to acquire and analyse data from every station, hence a smaller sample of 5 stations was selected for investigation. The stations in the sample are outlined in Table 2.2, a mixture of 2-detector and 4-detector stations. Approximately 110 of the  $\sim 140$  stations acquire singles rate data, which has only been available since 2016, and only 29 stations acquire weather data. In general throughout the history of the HiSPARC network, the availability of weather data is irregular and many stations that acquire the data go through periods of acquiring no meteorological data at all, which made the selection of stations non-trivial.

The 5 stations in the sample were selected as they generally all have both the singles and weather data available, with the exception of station 14001 (Birmingham University). Station 14001 only came online in 2014; it does not acquire weather data and did not begin acquiring singles data until February 2019, but it was deemed necessary to include this station as it is maintained by the University. Station 501 (Nikhef) is the original station in the network, and serves as the ‘gold standard’ for HiSPARC, therefore it was included. The other three stations all showed good data quality in terms of data availability and consistent operating conditions. The stations are shown on a map in Fig. 2.3.

Figure 2.4 shows the availability of CR data for the sample of stations for each of the space weather events investigated, where purple grids denote no available data, teal denotes events data were available, and yellow denotes events and singles data were available. It also shows as the HiSPARC network matures, so does the number of stations with available data, and the type of data available (both events



Figure 2.3: The geographic location of each HiSPARC station considered in this work. Each green circle denotes the location of a detector station.

and singles rates).

## 2.4 Station Properties

### 2.4.1 Cut-Off Rigidity

To understand the PCR spectrum that ground-based CR detectors are capable of observing, PCR transport simulations are typically performed. The geomagnetic field can allow or prohibit CR particles penetrating the magnetosphere and reaching the atmosphere, depending on the particle's energy. Transport simulations allow us to determine the range of PCRs that have sufficient energy to penetrate the Earth's magnetosphere and reach the atmosphere and produce secondary particle air showers. The PCR spectrum depends strongly on the geographic location of the station; the minimum allowed particle rigidity varies from  $\sim 17$  GV near the equator

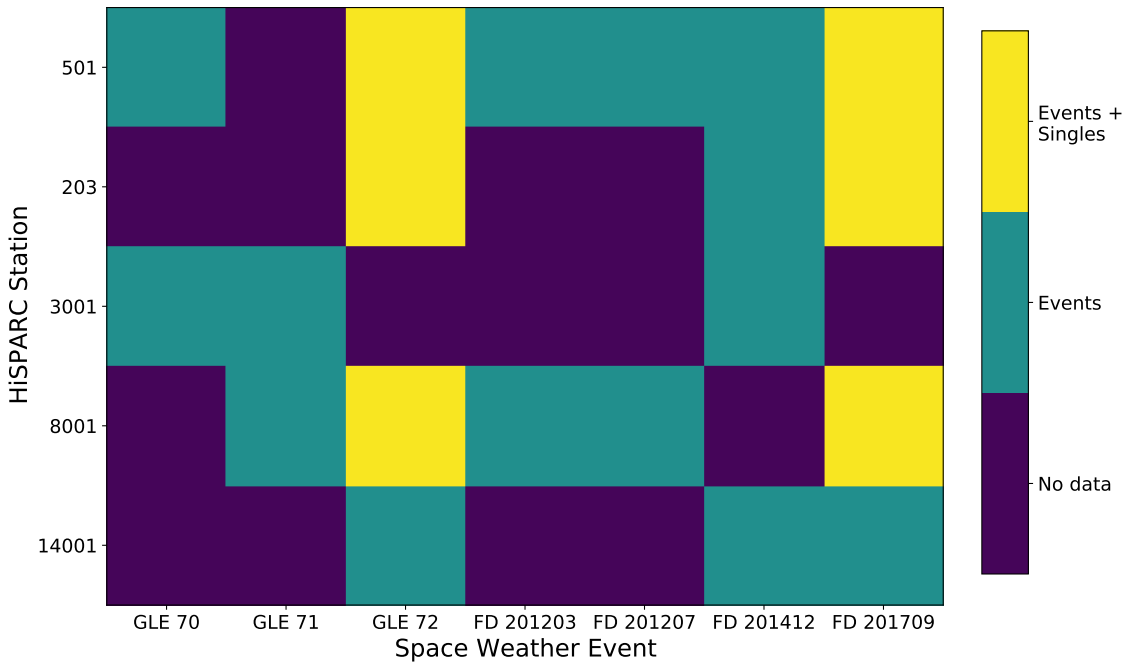


Figure 2.4: The availability of data for each HiSPARC station considered, for each of the space weather epochs listed in Table 2.1. The purple grids denote no available data, teal denotes that only the events data are available, and yellow denotes that both the events and singles data are available.

and theoretically 0 GV at the poles, and the geomagnetic conditions have a strong impact on the PCR spectrum ([Shea et al., 1965](#); [Desorgher, 2005](#); [Desorgher et al., 2006](#); [Danilova et al., 2019](#)).

Transport simulations typically run a reverse evolution of particles, using a backwards-tracing routine, whereby the particles are simulated from Earth out to the magnetosphere, to determine whether they leave the magnetosphere or remained trapped. In this work, to perform the PCR transport simulations we used the PLANETOCOSMICS software. PLANETOCOSMICS performs Geant4 Monte Carlo simulations of charged particle transport through Earth's magnetosphere based on Størmers transport equation for charged particles ([Desorgher, 2005](#); [Desorgher et al., 2006](#)). PLANETOCOSMICS simulates backward trajectories of charged particles from a given location (latitude, longitude, and altitude) out to the magnetopause for a set of PCR rigidities.

For each trajectory simulated there are two possible outcomes: (i) the particles

trace out to the magnetopause where they escape Earth's magnetosphere, an allowed trajectory; (ii) the particles are sufficiently bent by the effect of the Earth's magnetosphere that they do not reach the magnetopause and cannot escape the Earth's magnetosphere, a forbidden trajectory (Desorgher, 2005; Desorgher et al., 2006). The coordinates of the asymptotic direction at the magnetosphere are provided as an output to the simulations projected back down to the Earth's surface. In this work PLANETOCOSMICS was configured with the Tsyganenko-89 model for the external magnetospheric magnetic field and the International Geomagnetic Reference Field (IGRF) internal field model.

Each rigidity simulated, whether it was an allowed or forbidden trajectory was stored, was used to provide an insight into the rigidity spectrum for a given station. From the allowed trajectories the effective cut-off rigidity ( $R_C$ ) for the stations was computed, which represents the lower rigidity limit above which cosmic rays can cross the magnetosphere:

$$R_C = R_U - \sum_{i=R_L}^{R_U} \Delta R_i \quad (2.1)$$

where  $R_U$  is the upper rigidity (the last allowed trajectory before the first forbidden trajectory);  $R_L$  is the lower rigidity (the last allowed trajectory before which all other trajectories with a lower rigidity are forbidden);  $\Delta R$  is the rigidity step size in the simulation (Desorgher, 2005; Desorgher et al., 2006; Herbst et al., 2013).

The rigidity spectrum for each of the HiSPARC stations were investigated to determine  $R_C$  for each station. The cut-off rigidity calculated for the six HiSPARC stations for a vertical incidence upon the atmosphere (i.e.  $0^\circ$  zenith angle) are shown in Table 2.2 which show that there is little variation in  $R_C$  between the HiSPARC stations and that they observe protons with rigidities in excess of  $\sim 3$  GV. This analysis was initially carried out for the vertical direction (i.e. azimuth =  $0^\circ$ , zenith =  $0^\circ$ ); however further trajectories were simulated for different azimuth and zenith angles to determine the dependence of the rigidity spectrum on the detector

Table 2.2: Properties of some of the HiSPARC stations: geographic longitude ( $\phi$ ), geographic latitude ( $\lambda$ ), altitude ( $h$ ), and the geomagnetic vertical cut-off rigidity ( $R_C$ ) calculated from the PLANETOCOSMICS simulations.

Station Name/ID	$R_C$ [GV]	$\phi$ [deg]	$\lambda$ [deg]	$h$ [m]	No. Detectors
Nikhef/501	3.19	4.95 E	52.36 N	56.18	4
College Hageveld/203	3.18	4.63 E	52.35 N	53.71	2
Leiden/3001	3.23	4.45 E	52.17 N	54.08	2
Eindhoven/8001	3.44	5.49 E	51.45 N	70.12	2
Birmingham University/14001	3.06	1.93 W	52.45 N	204.14	4

acceptance angle. The analysis for the azimuthal dependence was carried out at a zenith angle of  $20^\circ$  as this is around the most probable angle for HiSPARC events, and the analysis of the zenith dependence was carried out at an azimuth angle of  $0^\circ$ .

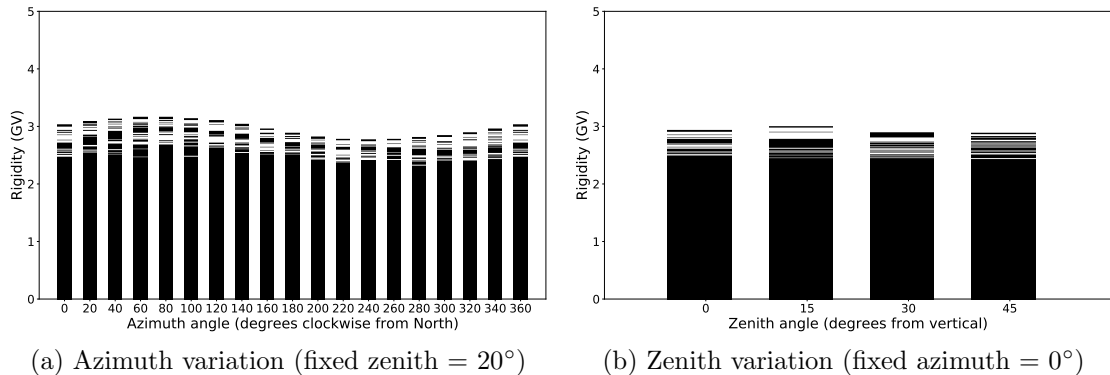


Figure 2.5: Azimuthal and zenith angle variations in the allowed and forbidden rigidity trajectories for HiSPARC station 501. The forbidden trajectories are in black.

The small variation between HiSPARC stations is due to their close proximity in geographic latitude and longitude. The values of  $R_C$  calculated for the HiSPARC stations suggest that they should be able to observe higher energy Solar Cosmic Ray (SCR), but may not be as susceptible as the higher latitude NM where the effects of GLEs are highly observable.

## 2.4.2 Asymptotic Viewing Directions

Another output from the PLANETOCOSMICS simulations allowed us to understand the directions of moving particles entering the Earth’s magnetosphere prior to their trajectory through the magnetosphere and arrival at the atmosphere. By tracking particles trajectories we can define the Asymptotic Viewing Direction (AVD) of CR stations which represents the direction of CR motion before entering the magnetosphere and being observed by a detector. This allowed us to understand the directions in space that ground-based CR detectors observe. Higher energy CRs are deflected less by the magnetosphere and therefore the AVDs of high rigidity cut-off stations are simply their zenith; however, lower energy CRs are deflected more, there stations with a lower rigidity cut-off may observe CRs from a range of directions.

It can be seen from Figure 2.6 that the AVDs for each of the HiSPARC stations investigated are rather similar, due to their close geographic proximity, and that they mostly straddle the equator for low rigidity PCRs.

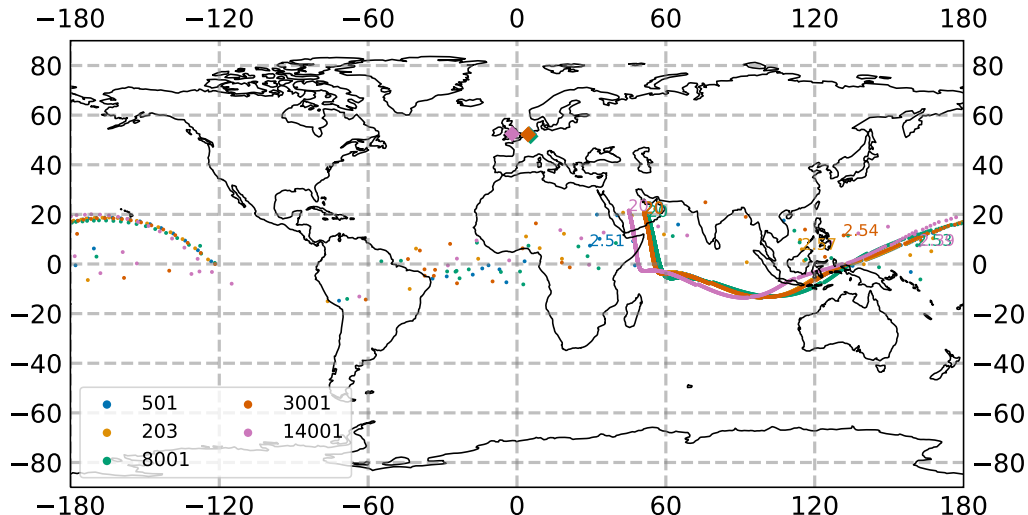


Figure 2.6: The vertical asymptotic viewing directions of 5 HiSPARC stations. The rigidity range of the simulations were from  $1.0 \text{ GV} < R < 20.0 \text{ GV}$ , and the results are plotted in geographic coordinates on January 20th 2005. The diamonds correspond to the HS ground location and the circles correspond to the AVD for a specific rigidity value.

The simulations were only performed up to a rigidity of 20 GV; however, at higher rigidities, we would see the AVDs spiral in towards the geographic location

of the station, and the PCR would enter the magnetosphere and atmosphere almost vertically above the detector. The 20 GV directions are all grouped closely together due to the stations' close geographic locations. This map of the AVDs also informs us that we should expect to be able to observe some lower energy PCRs when the zenith of the detector is not facing the asymptotic direction of the PCR. The viewing directions of lower energy CRs with  $R_C \sim 2.5$  GV are shifted East by  $\sim 120^\circ$  longitude, therefore may observe particles from this direction some  $\sim 8$  hours before the stations align with the direction of the source.

This has significant impacts on the ability of our detectors to observe transient solar eruptive events which may be highly anisotropic and have a Solar Energetic Particle (SEP) spectrum with energies  $< 10^9$  eV. For this reason, many ground-based CRs spread detectors across Earth's surface, to maximise their observation coverage.

## 2.5 HiSPARC Observations

It was highlighted during private communication with the UK Met Office that observations of GLEs are of more interest and importance to space weather forecasts and nowcasts – [probably add a comment here to relate this to the earlier onset of SEPs that will be observed by muon detectors...!!]. FDs are of lower interest and importance; however, we still searched for FDs within the HiSPARC data for completeness.

### 2.5.1 Observations of Ground Level Enhancements

The search for evidence of GLEs within the HiSPARC data was conducted for the GLEs listed in Table 2.1, as they are the only GLEs that span the operational epoch of the HiSPARC network. Figure 2.7, 2.8, and 2.9 show the HiSPARC observations around the epochs of GLE 70, 71, and 72, respectively. As highlighted by Fig. 2.4, most of the observations are only the events data (i.e. coincidences between the detectors of a station); however, where possible, we also show the singles rates from

each of the individual detectors in a station, when available.

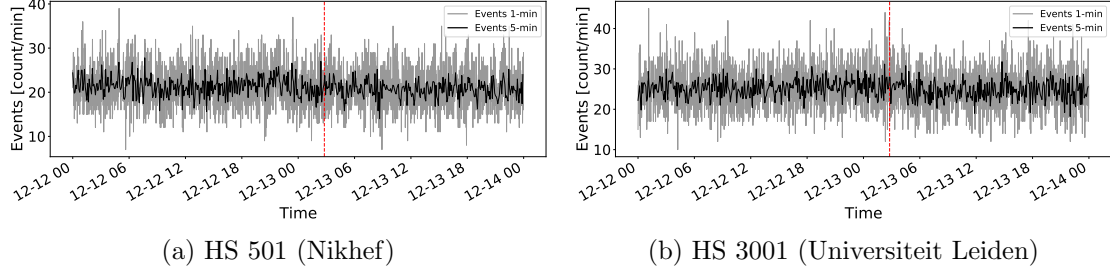


Figure 2.7: HiSPARC data for stations 501 and 3001 around the epoch of GLE 70 on 13/12/2006. The plot shows the minute-averaged and 5-minute-averaged trigger events between detectors within the station. The vertical red, dashed line depicts the approximate onset time of the GLE. The units of time on the x-axis are, MM-DD HH.

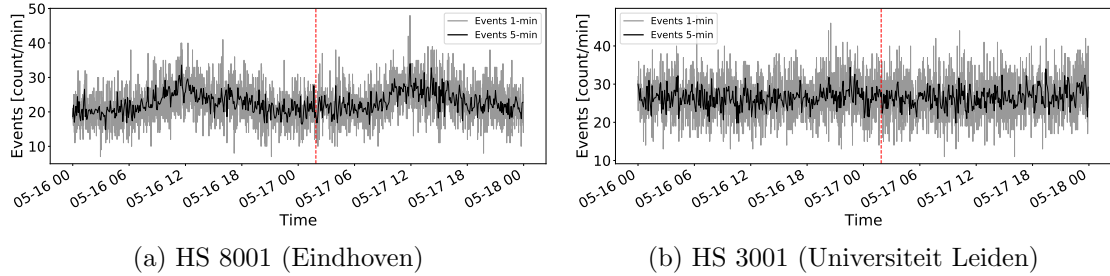


Figure 2.8: HiSPARC data for stations 8001 and 3001 around the epoch of GLE 71 on 17/05/2012. The plot shows the minute-averaged and 5-minute-averaged trigger events between detectors within the station. The vertical red, dashed line depicts the approximate onset time of the GLE. The units of time on the x-axis are, MM-DD HH.

We can see from Figures 2.7, 2.8, and 2.9 that there are no clear and obvious signs of the GLE signals in the HiSPARC observations, as for those given in Fig. 2.1 for the Oulu NM station, in Finland. This is the case for both the events data and the singles data.

There are some excursions from the mean count rate, this is significantly more prominent in the singles rates which are shown in the GLE 72 plots for stations 501, 203, and 8001. It was thought that these excursions are the effect of atmospheric pressure on the muon count rates; in Section 2.6 this is discussed further and the effect is accounted for. After its removal we then re-investigated the corrected data, which is discussed in Section 2.7.

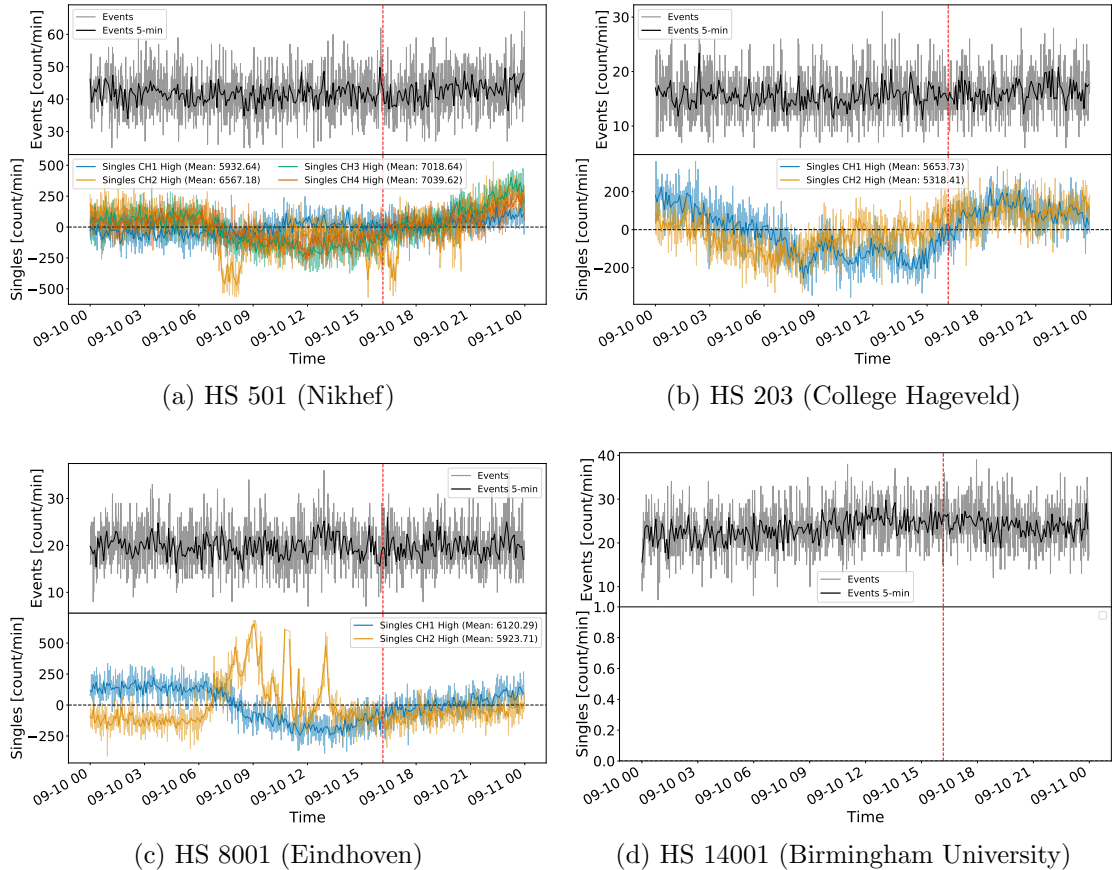


Figure 2.9: HiSPARC data for 4 stations around the epoch of GLE 72 on 10/09/2017. The top panel of each subplot shows the minute-averaged trigger events between detectors within the station, while the bottom panel shows the mean-shifted, minute-averaged counts by each individual detector in the station. The vertical red, dashed line depicts the approximate onset time of the GLE. The units of time on the x-axis are, MM-DD HH.

No clear GLEs have been observed in the HiSPARC data. We believe this is due, in-part, to the rigidity cut-off of the HiSPARC stations, as well as the different particle species observed by HiSPARC compared to the NMAs. GLEs are normally associated with SEPs with energies in the MeV-regime; hence typically GLEs are observed by NMAs. Only the most energetic have been observed by MDs as they are more sensitive to the hard component of the PCR spectrum. Observations of GLEs with HiSPARC will therefore only be linked with the maximum energy release during solar flares, and often this is very short and still of insufficient energy to be detected by MDs (McCracken et al., 2012; Augusto et al., 2016).

To further understand the impact of SEP energies on the HiSPARC observations,

in Section 2.6 we used simulations to investigate the CR spectrum at quiet times and during GLEs.

### 2.5.2 Observations of Forbush Decreases

The search for evidence of FDs within the HiSPARC data was conducted for the FDs highlighted in Table 2.1. Figure 2.10, 2.11, and 2.12 show the HiSPARC observations around the epochs of the first four FDs listed in Table 2.1. Each of the plots shows only observations using the HiSPARC events data (i.e. coincidences between the detectors of a station), as singles data was not available at those epochs (see Fig. 2.4).

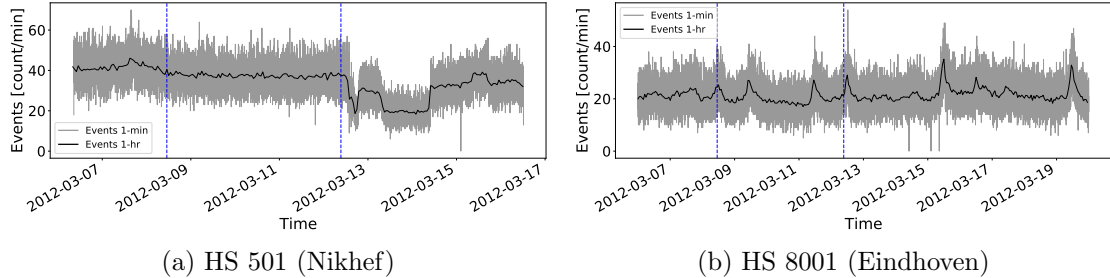


Figure 2.10: HiSPARC data for stations 501 and 8001 around the epoch of the FDs in March 2012. The plot shows the minute-averaged and hourly-averaged trigger events between detectors within the station. The vertical blue-dashed lines show the approximate onset-time of the FDs. The units of time on the x-axis are, YYYY-MM-DD.

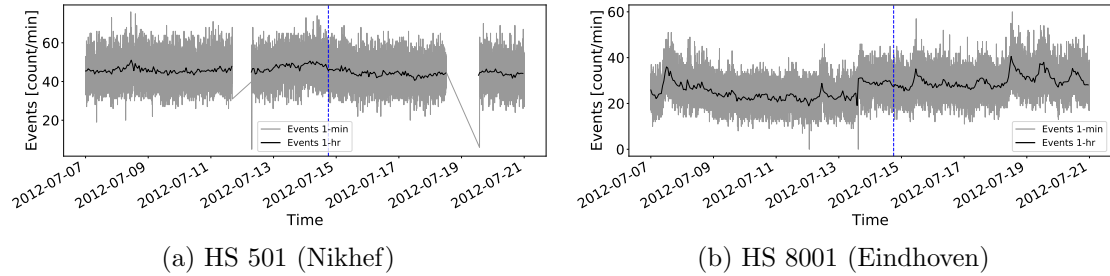


Figure 2.11: HiSPARC data for stations 501 and 8001 around the epoch of the FD in July 2012. The plot shows the minute-averaged and hourly-averaged trigger events between detectors within the station. The vertical blue-dashed line shows the approximate onset-time of the FD. The units of time on the x-axis are, YYYY-MM-DD.

We can see from the plots that there are no clear signs of the FD signals in the HiSPARC data shown here. We observed a set of significant decreases in the muon

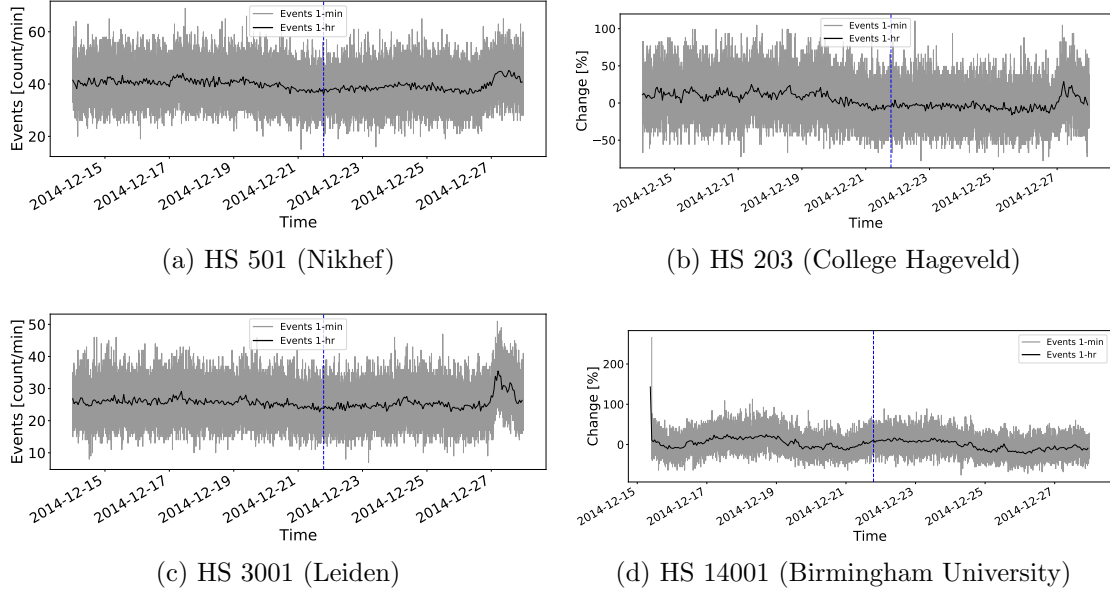


Figure 2.12: HiSPARC data for four stations around the epoch of the FD in December 2014. The plot shows the minute-averaged and hourly-averaged trigger events between detectors within the station. The vertical blue-dashed line shows the approximate onset-time of the FD. The units of time on the x-axis are, YYYY-MM-DD.

count rate in station 501 after the second FD in March 2012 (see Figure 2.10a); however, it is unclear whether this was a consequence of the FD or other hardware reasons, as the FD was not observed in the other HiSPARC station. The shape of the FD in the NM data shows a sudden decrease and a smooth recovery within two days, but the shape of the HiSPARC observations traces a more complex evolution, which suggests that the cause is not the FD, but rather a result of hardware.

As we saw with the earlier investigation into GLEs, we again see excursions from the mean count rate which vary over longer time scales. This is due to variations in the atmospheric pressure. In Section 2.6 this is discussed further and the effect is accounted for.

In addition, it is quite clear from Figure 2.10b and Figure 2.11b that station 8001 (Eindhoven) displays a semi-persistent diurnal variation in the count rate. We know that daily variation is a combination of the CR anisotropy in the interplanetary space and a consequence of the rotation of the Earth meaning detectors look in different directions over the course of a day; however, we typically expect this diurnal

variation to be  $< 1\%$  (Mishra & Mishra, 2007, 2008; Dubey et al., 2016; Thomas et al., 2017), but here we see an increase of  $\sim 100\%$ , which suggests there may be an additional factor due to another source, likely originating in hardware.

For the final two FDs listed in Table 2.1, the plot of the HiSPARC observations is shown in Figure 2.13. Plotted are the HiSPARC events data; however, where possible, we also show the singles rates from each of the individual detectors in a station, when available. Furthermore, as these FDs were precursory to GLE 72, we also marked on the epoch of the GLE for completeness.

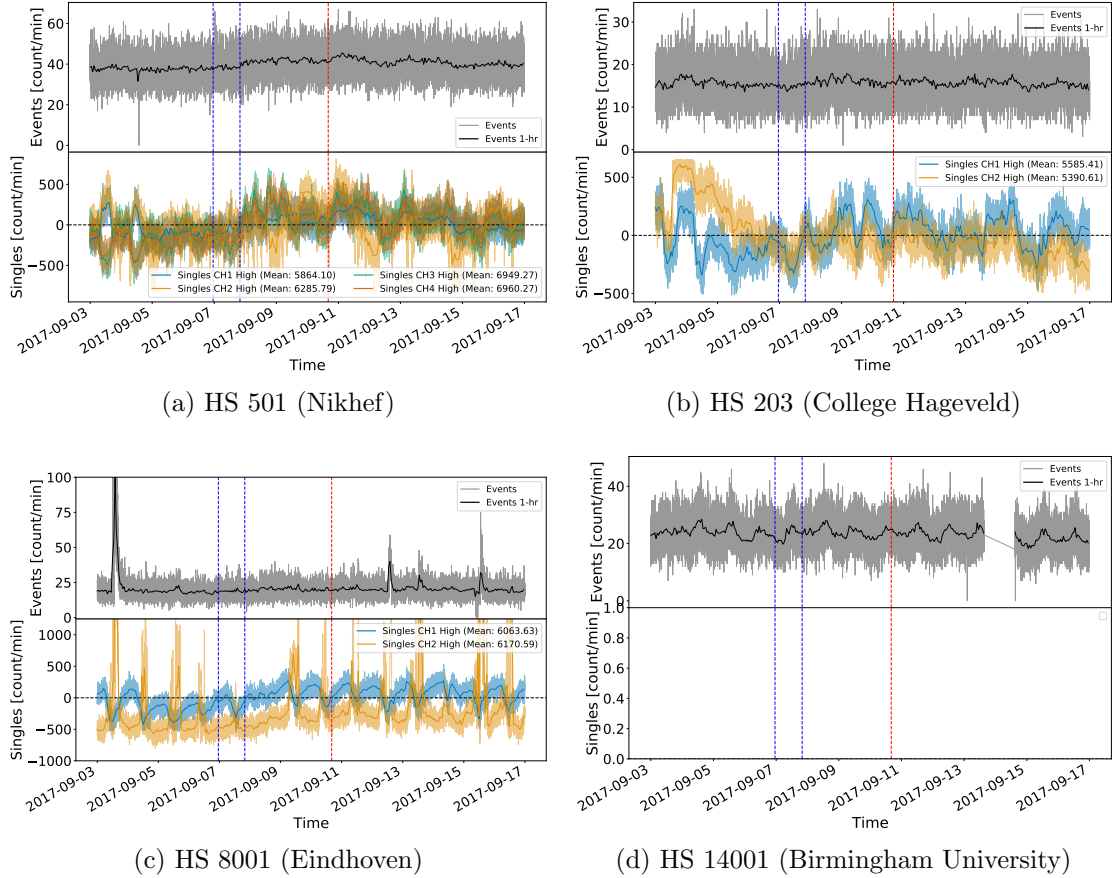


Figure 2.13: HiSPARC data for four stations around the epoch in which there were two FDs close to the onset of GLE 72. The top panel of each subplot shows the minute-averaged trigger events between detectors within the station, while the bottom panel shows the mean-shifted, minute-averaged counts by each individual detector in the station. The vertical blue-dashed lines show the approximate onset-times of the two FDs observed around this epoch and the red-dashed line depicts the approximate onset time of the GLE. The units of time on the x-axis are, YYYY-MM-DD.

As with the other FD epochs, we again do not observe any clear signs of the FD

signals in either the events nor singles data. In each of the three stations for which there were singles data, we observed a semi-persistent diurnal signal. This was also seen in the events data for station 14001. In the singles data we

Furthermore, we again observed a slow variation in the count rate which is suspected to be due to atmospheric pressure and is discussed in Section 2.6.2.

No clear signal of FDs has been observed in the HiSPARC data. We again believe this could be due to the rigidity cut-off of the HiSPARC stations. We also note that the atmospheric effects in the raw data do not help our ability to observe the space weather effects, therefore we make an effort in the next section to remove these effects and standardise the HiSPARC data.

## 2.6 Atmospheric Corrections of HiSPARC Data

### 2.6.1 Motivation

It is well known that observations made by ground-based CR detectors are susceptible to atmospheric conditions [ADD SOME REFS FROM ZOTERO]. As we have seen in the plots show in Section 2.5, there exist excursions in the data whose origins are from atmospheric variations. This sensitivity makes it difficult to differentiate variations due space weather events to those simply due to atmospheric conditions, therefore it was necessary to remove these effect from the data.

### 2.6.2 Barometric Correction

Atmospheric pressure effects the CR path length due to the expansion and contraction of the atmosphere with varying pressure ([Dorman, 1972](#); [Paschalis et al., 2013](#)); hence the CR counts are observed to be negatively correlated to atmospheric pressure as shown for both NMs and MDs in Figure 2.14.

A correction for this barometric effect is routinely applied as part of the data calibration for all NM stations within the Neutron Monitor Data Base (NMDB)

and an online barometric coefficient tool<sup>2</sup> is available for NMIs, which allows users to perform the barometric correction for a given station over a user-defined epoch (Paschalis et al., 2013). There is no such process routinely applied in the HiSPARC data pipeline.

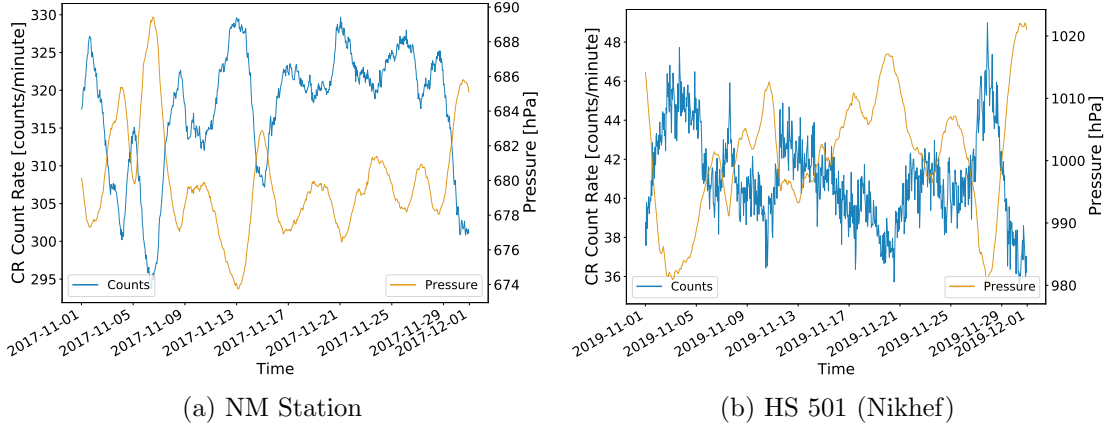


Figure 2.14: The anti-correlation between CR count rates and the atmospheric pressure. (a) shows the CR and the local atmospheric pressure measured at a NM in the South Pole; (b) shows the CR and pressure measured by HiSPARC station 501.

The method of correcting for the barometric effect is discussed widely in the literature regarding NMIs and is shown to depend on the barometric coefficient. Assuming the cosmic ray flux variation, absent of the atmospheric effects, is reasonably stable, then a simple correction to the counts can be made. The CR variations ( $N$ ) that depend on the local atmospheric pressure are described by:

$$\Delta N = -\beta N \Delta P, \quad (2.2)$$

where  $\Delta N$  is the change in count rate,  $\beta$  is the barometric coefficient, and  $\Delta P = P - P_0$  is the deviation in pressure from the average ( $P_0$ ) in the given time-period (Paschalis et al., 2013)

Through the integration of equation (2.2), the solution shows the dependence of cosmic ray intensity on pressure,

---

<sup>2</sup><http://cosray.phys.uoa.gr/index.php/data/nm-barometric-coefficient>

$$N = N_0 e^{-\beta \Delta P}. \quad (2.3)$$

Therefore by taking the logarithm of equation (2.3), one can obtain the barometric coefficient by fitting the linear model to the observed data, in the form:

$$\ln \left( \frac{N}{N_0} \right) = -\beta \Delta P, \quad (2.4)$$

where  $N_0$  may be assumed as the mean count rate over the given time-period of observations considered.

A demonstration of this method is shown for both a NM and a HiSPARC station in Figure 2.15. In both cases the linear fit does a good job of finding the barometric coefficient and was used to remove the pressure effect from the data... (probably should show a plot of the before vs after for either the hisparc or the nm data too...?)

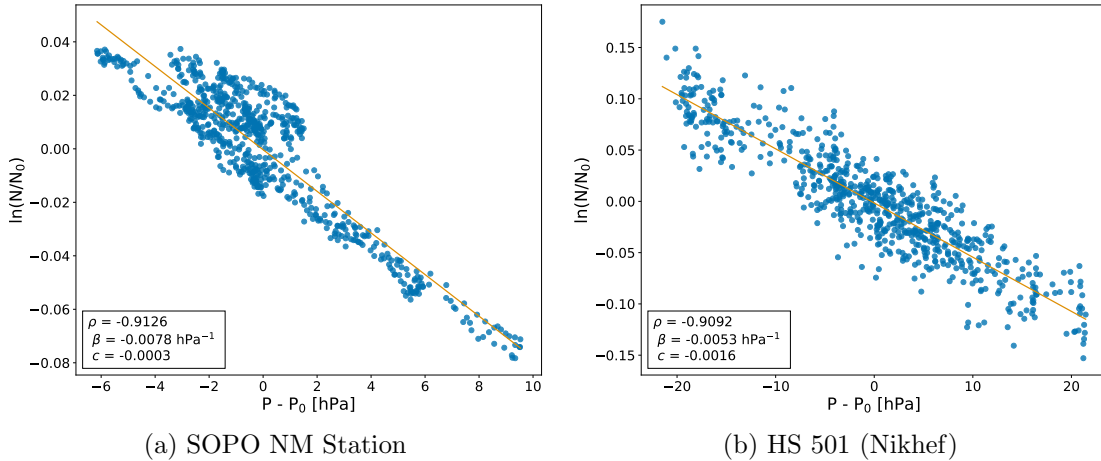


Figure 2.15: The barometric coefficient calculation: (a) during November 2017 for the South Pole (SOPO) NM station, (b) during November 2019 for HiSPARC station 501 at Nikhef.

Using the online barometric coefficient tool ([Paschalis et al., 2013](#)), it was possible to provide a comparison between the method used in this work to that which is used for the correction of the NMDB stations. This is provided in Figure 2.16 for monthly corrections throughout 2017 for the NM station at the South Pole (SOPO).

Figure 2.16 shows a close agreement between the barometric coefficient calculated

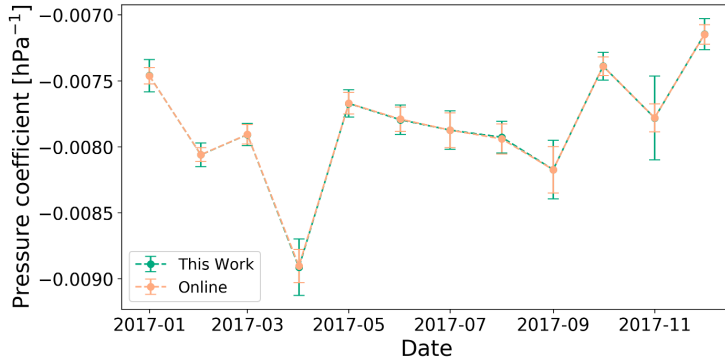


Figure 2.16: A comparison between the monthly barometric coefficient computed in this work and using the online barometric coefficient tool throughout the year 2017 for the SOPO NM station.

in this work and those acquired from the online tool for the SOPO NM. This was also true for other stations tested (APTY and ROME), thus providing confidence that the method used in this work was suitable for application on the HiSPARC data.

As this method has been shown to reproduce the results of the NMDB corrections the barometric correction was performed on the stations where sufficient pressure data and count rates exist, and were re-investigated to determine whether the space weather events were observed in the HiSPARC data. These results are provided in Section 2.7.

[include a time series for the variation in the barometric coefficient for HiSPARC (i.e. for station 501)...???

### 2.6.3 Temperature Correction

It has been discussed in the literature that the effect of atmospheric temperature on muon intensity has to be treated differently to the pressure effect ([Berkova et al., 2011](#)), as the temperature influences both the creation and disintegration processes for muons, such that there is a positive effect and a negative effect on muon intensity as a consequence of temperature variations ([Mendonça et al., 2016](#)).

The positive effect is related to pion decay and its dependence on temperature variation. The higher the temperature, the lower the atmospheric pion absorption,

which implies a higher generation rate of muons ([Mendonça et al., 2016](#)).

The negative effect corresponds to the decrease of muon intensity at ground level as the muon average path length varies with temperature. Due to the heating and the expansion of the atmosphere during summer periods muons are produced higher in the atmosphere; hence the muon propagation path increases meaning more atmosphere for muons to traverse before reaching the ground, and an increased decay probability and ionisation losses ([Savi et al., 2015](#); [Mendonça et al., 2016](#)).

Due to the difference in decay probability, the negative effects dominate for low energy muons (i.e. those detected by ground-level MDs), and the positive effect dominates for high energy muons (i.e. those detected by underground MDs) ([Berkova et al., 2011](#)); therefore it is expected that the negative effect should dominate for the HiSPARC network. This is in contradiction with the observations of diurnal variation with the HiSPARC detector, as one can quite clearly see that the HiSPARC stations register higher count rates during local noon (see Fig. 2.9c). However, when observing the singles rates, we do see some detectors displaying a positive effect and some displaying a negative effect (see Fig. 2.9), so this is not consistent throughout each station, and provides more evidence to suggest this is an effect of thermally induced noise in the Photo Multiplier Tubes (PMTs).

Several methods of correcting for the temperature effect are discussed in the literature, see [Berkova et al. \(2011\)](#); [Mendonça et al. \(2016\)](#) for a summary. However, the methods discussed are typically applied over long timescales of years with low temporal resolution, rather than to account for short timescale variations with periods of less than a day; hence these methods aren't necessarily suitable for this work on ephemeral space weather events.

The HiSPARC stations provide the local outdoor temperature which is measured nearby the detectors, and also the temperature in the room where the electronics are located. The latter is not of use, but the former can be used for temperature corrections. Figure 2.17a shows the pressure corrected events data and the temper-

ature data for station 8001 in July 2012. There is a strong correlation between the events and the temperature, which is shown in Figure 2.17b. Despite the literature, we used the same linear fitting technique described for the pressure correction in Section 2.6.2; however, replacing the pressure for locally measured outdoor temperature.

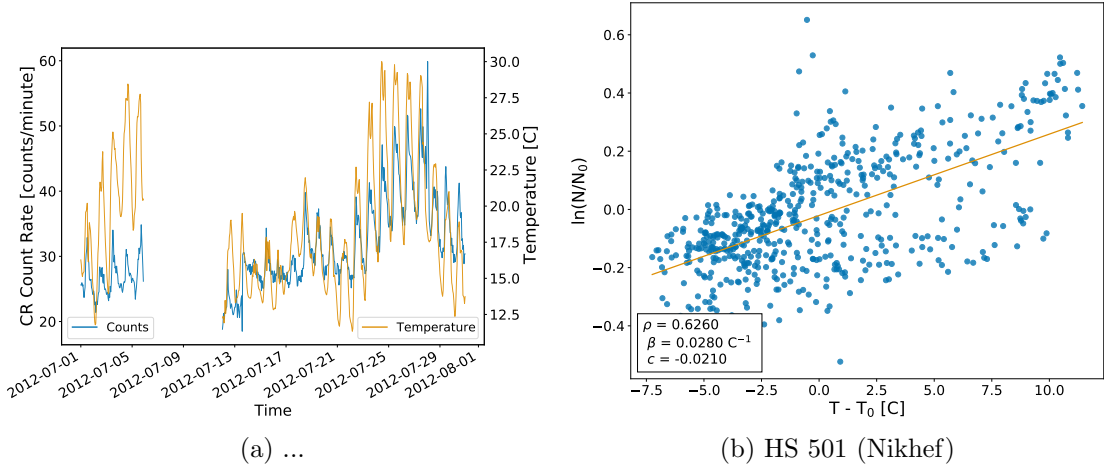


Figure 2.17: ...

(probably should show a plot of the before vs after for either the hisparc or the nm data too...?)

## 2.7 HiSPARC Observations After Atmospheric Corrections

### 2.7.1 Observations of Ground Level Enhancements

Following the atmospheric correction, the search for evidence of GLEs was re-conducted, this time within the corrected HiSPARC data. This could only be conducted for GLE 71 and 72, as the HiSPARC network was not collecting meteorological data during the epoch of GLE 70. Figure 2.18 and Figure 2.19 show the atmospheric-effect corrected HiSPARC observations around the epochs of GLE 71 and 72, respectively. The observations of GLE 71 show only the HiSPARC events

data; however, we also show the singles rates from each of the individual detectors in a station for GLE 72.

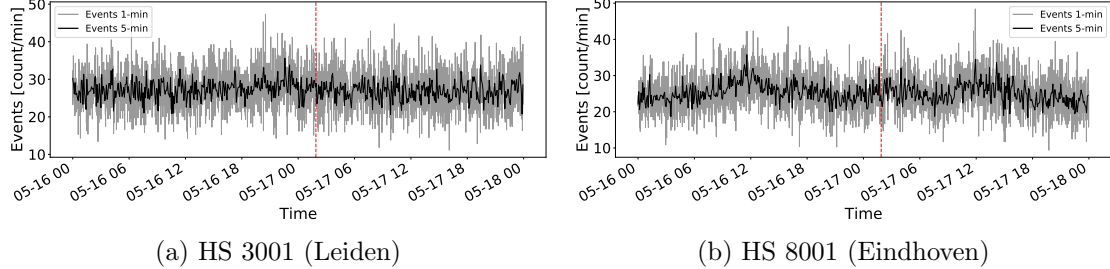


Figure 2.18: Atmospheric-corrected HiSPARC data for 2 stations around the epoch of GLE 71. The top panel of each subplot shows the minute-averaged trigger events between detectors within the station, while the bottom panel shows the mean-shifted, minute-averaged counts by each individual detector in the station. The vertical red, dashed line depicts the approximate onset time of the GLE.

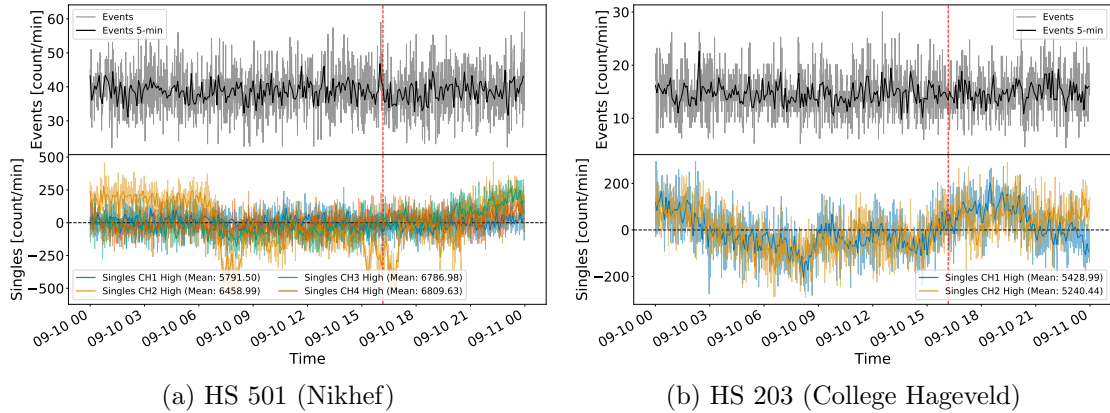


Figure 2.19: Full atmospheric-corrected HiSPARC data for 2 stations around the epoch of GLE 72. The top panel of each subplot shows the minute-averaged trigger events between detectors within the station, while the bottom panel shows the mean-shifted, minute-averaged counts by each individual detector in the station. The vertical red, dashed line depicts the approximate onset time of the GLE.

Despite the atmospheric correction, in general, doing a good job at removing atmospheric variations in the CR counts, there still remained no clear GLEs observations in the pressure corrected HiSPARC data. We believe this is due to the a mixture of the reasons discussed above: a high rigidity cut-off of the HiSPARC stations leading to a low increase in the CR count, as GLEs are typically caused by SEPs with a lower energy; hence too few additional muons were produced during the

GLEs. In addition, as discussed above, the events data require a trigger between 2 detectors that are separated by up to 10 m, therefore this further biases the stations to be sensitive to more energetic PCRs.

This provides motivation to investigate the flux of muons at ground level during quiet periods, i.e. from Galactic Cosmic Rays (GCRs), compared to the flux of muons at ground level during energetic solar events such as GLEs. This work was performed and is discussed Section 2.8.

### 2.7.2 Observations of Forbush Decreases

The search for evidence of FDs was also re-conducted using the atmospheric-effect corrected HiSPARC data. Figure 2.20 and Figure 2.21 shows the corrected HiSPARC observations around the epochs of a FD in July 2012 and December 2014, respectively.

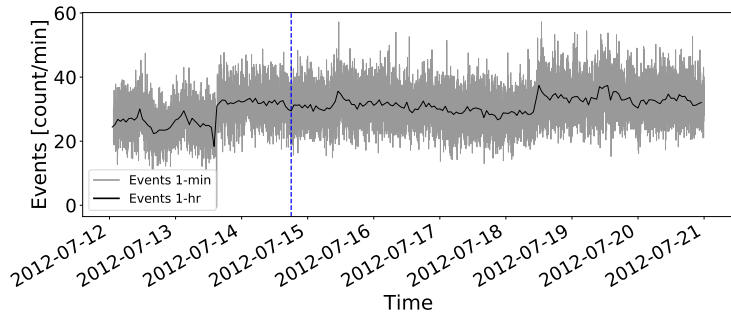


Figure 2.20: Full atmospheric correction of HS 8001 (Eindhoven) data during...

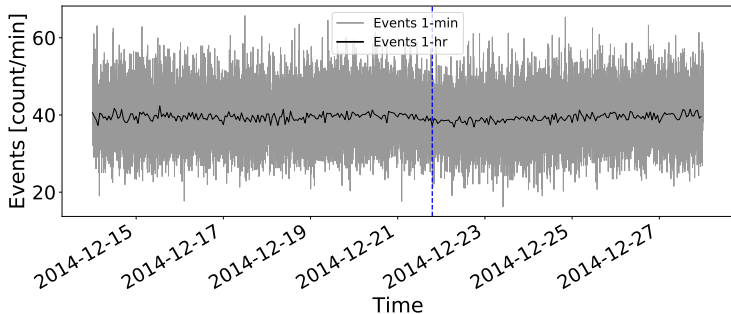


Figure 2.21: HS 501 (Nikhef)

In Figure 2.20 there is no clear FDs observation in the corrected HiSPARC data; however, Figure 2.21 there is a slight indication of a  $\sim 2\%$  decrease in the count

rate at the epoch of the expected FD. This suggests that after correcting the data for atmospheric effects, that FDs on the order of  $\sim 2\%$  may be observed by the HiSPARC network.

Finally, the atmospheric-effects corrected observations of the two FDs which occurred around GLE 72 is shown in Figure 2.22, showing the corrected events data and singles data for each of the individual detectors in the stations.

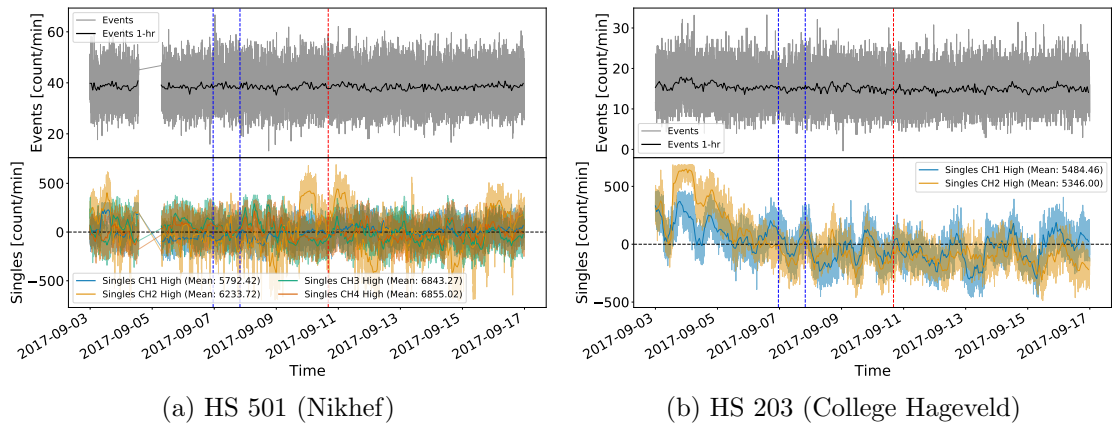


Figure 2.22: Pressure corrected HiSPARC data for 2 stations in an epoch where there were two FDs close to the onset of GLE 72. The top panel of each subplot shows the minute-averaged events data, while the bottom panels show the mean-shifted, minute-averaged counts by each individual detector in the stations. The vertical blue-dashed lines show the approximate onset-times of the FDs and the red-dashed line depicts the approximate onset-time of the GLE.

There are no clear FDs in Figure 2.22, and the singles plots demonstrate that the atmospheric corrections do not sufficiently remove all the signal excursions from the mean, and there remain large (up to 10%) deviations in the signals. This highlights that although the method of atmospheric corrections does work, it does not always. One reason for this, particularly for the singles, is that the measured temperature is recorded in the atmosphere and not inside the roof boxes containing the PMTs. The roof boxes are made of plastic and one would suspect the air temperature inside the boxes is different to the ambient atmospheric temperature measured nearby. In order to fully remove the effects of thermally induced count variations, we must record the more accurate temperatures of the PMTs instead of just the atmospheric

temperature.

## 2.8 Air Shower Simulations

### 2.8.1 Motivation

We have shown that no evidence that GLEs were observed in the HiSPARC data, even after correcting for atmospheric effects of pressure and temperature on the data. This leads us to question whether it is possible to observe GLEs with the HiSPARC detectors. In order to answer this, we needed to understand the muon flux at ground level and the scale of air shower footprints produced by PCRs. To investigate this, simulations of air shower development were performed for a range of PCRs energies for both primary protons and  $\alpha$ -particles.

To simulate the CR air shower development, the Cosmic Ray Simulations for Kascade (CORSIKA) software was employed: a Monte Carlo programme providing detailed simulations of the evolution of air showers initiated by PCRs through the atmosphere ([Heck & Pierog, 2017](#)). The particles in the CORSIKA simulations are tracked through the atmosphere until they undergo interactions with atmospheric nuclei, decay due to their instability, or reach the ground level defined as the simulation terminator.

Proton and  $\alpha$ -particle initiated air showers were generated with energies ranging from  $10^9$  to  $10^{20}$  eV, and  $4 \times 10^9$  to  $10^{20}$  eV, respectively. In total  $\sim 2 \times 10^5$  proton-initiated showers were simulated and  $\sim 2 \times 10^5$   $\alpha$ -particle-initiated air showers were simulated. Lists detailing the breakdown of PCR energies and number of simulations is provided in Appendix ??, along with a brief discussion of the settings chosen within the simulations.

### 2.8.2 Air Shower Footprints

The average footprint of the muons at ground level, due to PCRs, was calculated from the output of CORSIKA simulations. This was achieved by taking the distri-

bution of the number of muons at ground level at the end of the simulations as a function of their distance from the shower core, as this distance is provided as an output from the simulations. Multiple realisations of the air showers were simulated (see Table ??). For a given PCR energy, the mean distribution of radial footprints was calculated by averaging over all of the individual simulations. Figure 2.23 shows the radial distribution of muons at ground level for air showers induced by vertically incident protons and  $\alpha$ -particles.

In addition to the vertically induced air showers, we also repeated the simulations for air showers randomly selected from a uniform distribution of incident angles between  $0^\circ$  (vertical) and  $70^\circ$ , to provide a simulation that is more physically representative of CRs arriving from all directions. Radial distributions of muons were produced, similar to those in Figure 2.23, but they are not shown here as the difference is not drastically different by-eye.

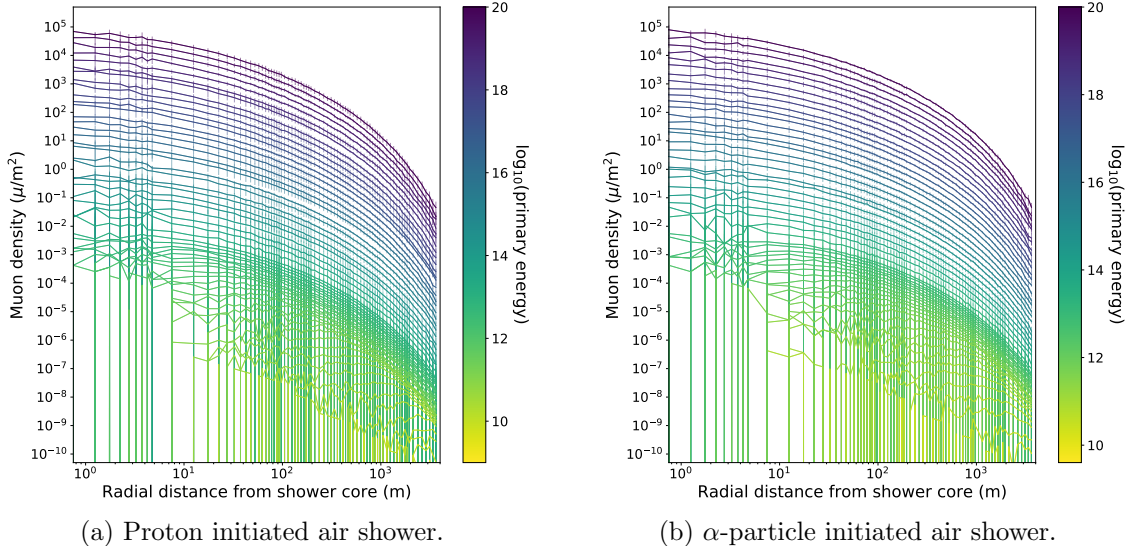


Figure 2.23: Mean muon density footprints for (a) proton-initiated air showers and (b)  $\alpha$ -particle-initiated air showers with initial PCR trajectories with zenith angles  $\theta = 0^\circ$  and various PCR energies. The error bars given represent  $1\sigma$ .

The interpretation of Figure 2.23 provides an understanding of the minimum energy PCRs observable by the different stations within the HiSPARC network. The typical separation between the detectors in a HiSPARC station is  $\sim 10$  m; however,

the separation between detectors varies from station-to-station and can be up to as much as some 20 m or as low as just a couple of metres. From these simulations we inferred that the variation in PCR energy sampled varies marginally over this range of HiSPARC detector separations and suggests that HiSPARC stations will typically observe PCRs with an energy on the order of  $\sim 10^{15}$  eV and above, as they produce a sufficient density of muons to meet the required trigger conditions of HiSPARC. This agrees with what was found by [van Dam et al. \(2020\)](#).

This helps to explain why the GLEs and FDs were not observed in the HiSPARC events data. The effects of GLEs and FDs are more prominent at lower PCR rigidities and the air showers induced by the lower rigidity PCR [PROBABLY NEED TO DROP SOME CITATIONS IN HERE!!] are not sufficient to induce an air shower that will trigger multiple detectors in a station. We see that lower energy PCRs do not produce EASs, but rather a very diffuse scattering of muons reach ground level. It is therefore clearer why we did not observe any GLEs in the events data, as the SEP-induced muons are insufficiently spread to trigger multiple detectors in coincidence. It would have been more likely to have observed GLEs in the singles data, as this only records the count rate of an individual detector. For a single 1 m x 0.5 m detector, we typically expect to observe PCRs with an energy on the order of  $\sim 10^{14}$  eV However, again they were not observed, which may be explained looking at the flux of muons at ground level.

### 2.8.3 Muon Flux

Another output from the CORSIKA simulations was the energy of the muons that reach ground level. From the air shower simulations it was therefore possible to compute an estimate of the energy distribution of the number of muons produced per PCR. Figure 2.24 shows the energy distribution of muons produced per primary PCR, for air showers induced by vertically incident protons and  $\alpha$ -particles.

The vertically incident air showers provides an upper boundary on the muon

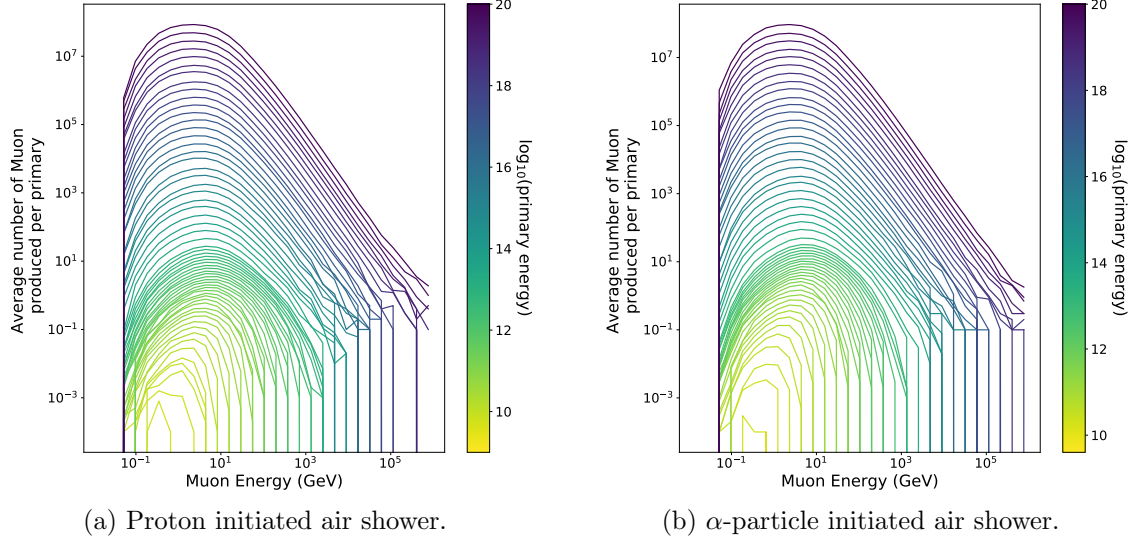


Figure 2.24: Mean number of muons produced at ground level by the PCR for (a) proton-initiated air showers and (b)  $\alpha$ -particle-initiated air showers, for various PCR energy.

flux, but we also repeated the simulations for air showers randomly selected from a uniform distribution of incident angles between  $0^\circ$  (vertical) and  $70^\circ$ , to provide a more physically representative flux. Similar plots were produced to those in Figure 2.24, but they are not shown here, as the difference is not drastically different by-eye.

We see from this analysis that PCRs with an energy less than  $\sim 10^{11} - 10^{12}$  eV produce on the order of only one muon that reaches ground level, and below this PCRs energy, it is rare that any muons arrive at ground. This helps explain why the GLEs were not observed in the HiSPARC events data. The effects of GLEs and FDs are more prominent at lower PCR rigidities, i.e. energies  $< 10^9$  eV. The air showers induced by the lower rigidity PCRs are not sufficient to produce significant variations in the flux of the muons at ground level, thus we do not observe a variation from the typical SEPs that induce GLEs.

We also used the data from the simulations to estimate the total muon flux at ground level, based on the PCR flux at the top of the atmosphere. We used a model for the GCR flux at Solar Maximum (Corti et al., 2019), which utilised measurements from the Alpha Magnetic Spectrometer (AMS-02) on-board the International Space

Station (ISS). Figure 2.25 shows the computed differential flux of muons at ground level, based on the simulations of vertically incident PCRs and those randomly simulated within a  $70^\circ$  acceptance cone.

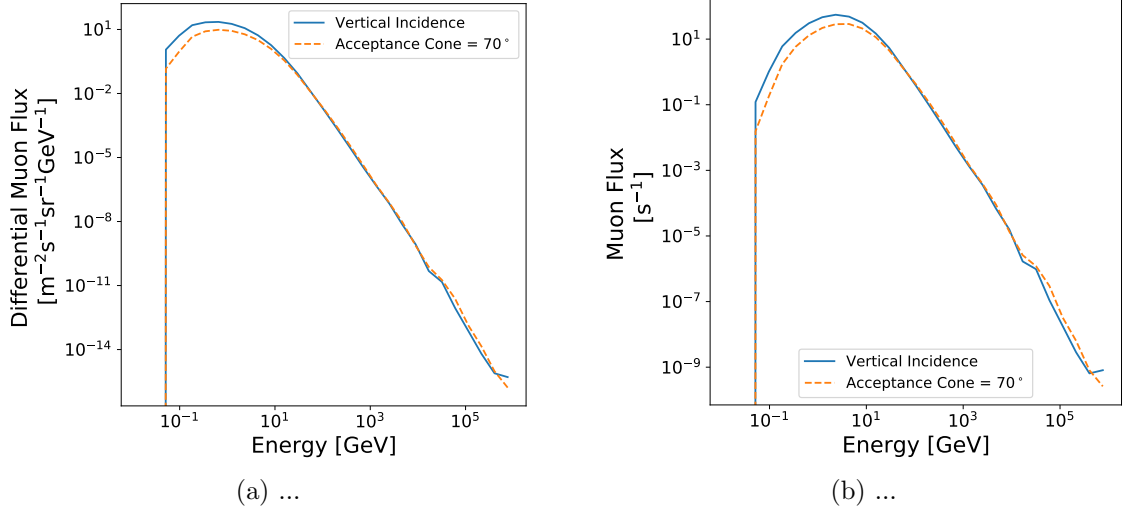


Figure 2.25: ...

From Figure 2.25, we see that the ground-based flux is similar for both types of simulation performed. In both, the low-energy muon flux dominates, and peak at a muon energy of  $\sim 1$  GeV.

Finally, we used these calculated spectra to determine the expected rate of muons passing through a single HiSPARC detector. We computed the rates as:  $85.365 \mu/\text{s}$  (for non-vertical, i.e.  $70^\circ$  acceptance cone simulations), and  $156.924 \mu/\text{s}$  (for vertical simulations). These rates are comparable to the generally accepted, average ground level muon flux on the order of  $\sim 1$  per  $\text{cm}^2$  per second ([Blackmore et al., 2015](#); [Pereira et al., 2020](#)).

To understand, from the CORSIKA simulations, how the count rate changed during a GLE, we required the PCR spectrum during these events. This information is not so easily acquired; however, there is a tool which provided muon fluxes based on the GCR spectrum and also GLE spectra, which is described in the next section.

## 2.8.4 Muon Flux From MAIRE

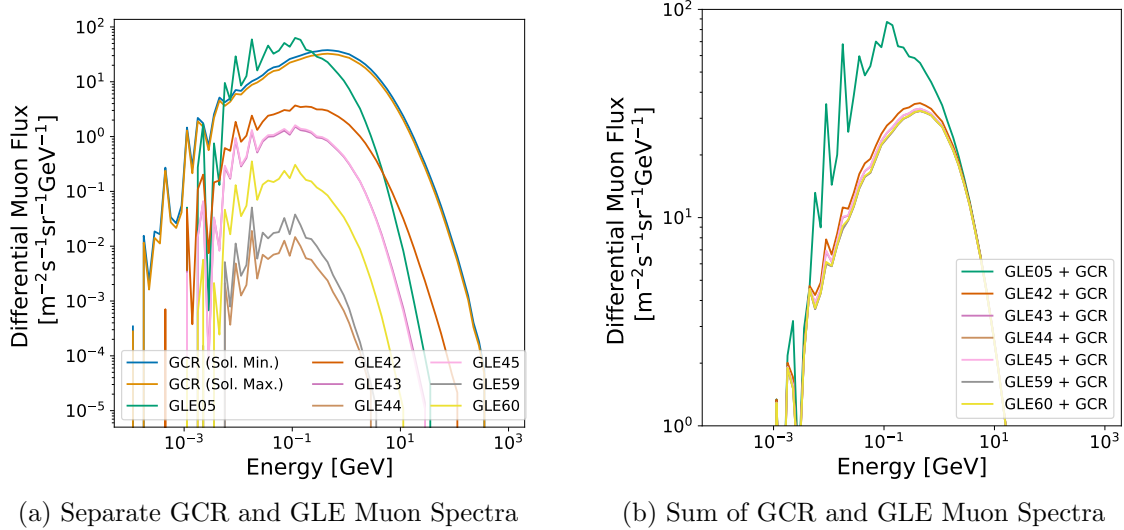
As a further comparison, we used the online Model for Atmospheric Ionising Radiation Effects (MAIRE) tool to compute the muon spectrum at ground level. MAIRE allows the computation of the secondary particle spectra in the atmosphere, caused by SEPs, including the ground level neutron and muon fluxes. MAIRE has an advantage of also having the PCR spectra for a number of GLEs built-in; however, they are for the strongest GLEs to-date. The GLEs within the MAIRE tool are detailed in Table 2.3, also providing the maximum increase in count rate, as observed in the NMDB, as a reference.

Table 2.3: The seven GLEs where MAIRE muon spectra were available, and the maximum observed increase in the neutron flux in the NMDB and the station where the increase was observed.

GLE	Date	Max. % change (station)
5	23/02/1956	~ 5100% (Leeds)
42	29/29/1989	~ 340% (Calgary)
43	19/10/1989	~ 90% (South Pole)
44	22/10/1989	~ 190% (McMurdo)
45	24/10/1989	~ 200% (South Pole)
59	14/07/2000	~ 60% (South Pole)
60	15/04/2001	~ 220% (South Pole)

The GLEs incorporated in the MAIRE tool predate the existence of the HiSPARC network; as a result, the simulations are not directly informative on the GLEs we were investigating in Table 2.1. Nevertheless, the MAIRE simulations helped in our understanding of whether it is likely that we could observe a GLE with the HiSPARC network.

We first use the MAIRE tool to simulate the spectra for the background GCRs and the seven GLEs at the Nikhef (501) HiSPARC station. Figure 2.26 shows the muon spectra for the GCR spectrum at solar minimum, and the additional muon spectrum for seven of the largest GLEs to date (which are additive to the GCR spectrum).



(a) Separate GCR and GLE Muon Spectra      (b) Sum of GCR and GLE Muon Spectra

Figure 2.26: Plots of the calculated MAIRE muon spectra for different incident spectra. Blue and orange lines show muon spectra calculated for the incident GCR spectra during solar minimum and maximum, respectively. The other coloured lines show the computed muon spectra for the incident GLE spectra. (a) shows the individual muon spectra for GCRs and GLEs; (b) shows the combined muon spectra for the GCR at solar maximum and the GLEs.

The GCR-induced muon spectrum in Figure 2.26 roughly agrees with that computed using CORSIKA, which gives us confidence in the results of both simulations. We can see that the effect on the muon spectrum drastically varies for the seven GLEs, with GLE 5 clearly the largest event.

Prior to inferring any conclusions about the muon spectra at the HiSPARC stations, as the MAIRE tool provides the neutron flux, we verified the accuracy of the MAIRE results by comparing the observed increases in NM count rates to those predicted by MAIRE. To reduce the effects of strong anisotropy when comparing to HiSPARC, we chose to analyse the NM count rate at a mid-latitude station, Kiel, which is located in Germany and is the nearest NM to the HiSPARC network. The properties of the Kiel station are:  $R_C=2.36$  GV, Altitude=54 m, Latitude=54.34°N, Longitude=10.12°E ([NMDB, 2018](#)).

Table 2.4 shows a comparison between the observed neutron count increase, measured using data from the NMDB, and the increases predicted by MAIRE. The Kiel NM station was not online in 1956, during the epoch of GLE 5, therefore this

event has been omitted from these results. The MAIRE increases were calculated by comparing the integrated GLE flux to the integrated background GCR flux at that epoch, including the effects of the disturbances in the Earth’s magnetic field from the planetary K-index ( $K_p$ ). In addition, the muon count increases predicted by MAIRE are also shown in Table 2.4, for comparison.

Table 2.4: Observed and predicted increases in the CR count rates at the Kiel NM station. The observed neutron increases use data from the NMDB, where the errors are the measurement uncertainty from the 5-minute averaged data. The predicted data for the neutrons and muons are from the MAIRE simulations. The ratio column provides a conversion factor from the MAIRE predicted neutron increases compared to those observed.

GLE	Neutrons Increase			Muons Increase
	Observed	Predicted	Ratio	Predicted
5	-	-	-	-
42	$\sim 160 \pm 5\%$	88.7%	1.80	3.98%
43	$\sim 19 \pm 1\%$	59.6%	0.32	0.790%
44	$\sim 6 \pm 1\%$	2.6%	2.30	0.00376%
45	$\sim 45 \pm 2\%$	67.9%	0.66	0.817%
59	$\sim 8 \pm 1\%$	6.1%	1.32	0.00906%
60	$\sim 24 \pm 2\%$	18.8%	1.28	0.0814%

We can see from Table 2.4 that there is a stark contrast between the observed NM increase and that predicted by MAIRE. One possible cause is, of course, inaccuracy in the predictions; however, more likely it is due to the anisotropy of the GLEs, as MAIRE does not adequately account for anisotropy in the simulations (Dyer et al., 2003; Lei et al., 2004). The ranked ordering from strongest to weakest GLEs in the observed Kiel data and that predicted by MAIRE are in good agreement, suggesting that despite an incorrect amplitude of the increase, generally the 2 data sets agree on which GLEs were the strongest. The ratio column gives a factor to convert from the MAIRE predicted increase to the NMDB observed increase. This therefore necessary as a calibration factor, to ensure that there is agreement between the MAIRE predictions and the observed data. Furthermore, as the ratio provides us with a calibration to recover the observed increase in neutron counts from the MAIRE simulations, we assume the same calibration factor can be applied to the

predicted increase in muon count. This conversion is shown in Table 2.5. In addition, Table 2.4 shows the significantly lower predicted muon increase, compared to the increase in neutrons. We know this is due to the energy spectrum of the PCRs, but the values in Table 2.4 provides further evidence to show that we may be unable to observe weaker GLEs.

We calculated the increase in muon count rate at several HiSPARC stations, and the predicted rates adjusted by the ratio in Table 2.4. These calculations relied on the assumption that the anisotropy does not have a significant effect on the increase observed between the Kiel NM station, and the HiSPARC stations in the Netherlands and the UK. The predicted count rates, adjusted for the factors in Table 2.4, are shown in Table 2.5. Again, GLE 5 has been omitted from these results as the Kiel station was not online then, so we cannot calibrate the MAIRE predictions.

Table 2.5: The MAIRE predicted increase in the muon flux, adjusted for the calibration factor between observed and predicted neutron increases at the Kiel station, in Table 2.4.

GLE	Predicted Muon Increase		
	Kiel	HS 501	HS 14001
5	-	-	-
42	7.18%	7.15%	7.33%
43	1.42%	1.40%	1.47%
44	0.00678%	0.00435%	0.00550%
45	1.47%	1.44%	1.53%
59	0.0163%	0.0102%	0.0123%
60	0.147%	0.139%	0.146%

The predicted increase in the muon count rates, calculated using the MAIRE simulations, for the NM station and the HiSPARC stations, in both the Netherlands and the UK, are in near-agreement. Assuming the effects of anisotropy are small, this suggests that the predicted spectra at the HiSPARC stations (adjusted for the calibration factor) are representative of the true increase one would expect to observe.

The effects of the GLEs show only a small increase in the muon count rate, and

for most of the GLEs, only contributes an increase of  $< 2\%$  in the ground-level muon flux, and generally  $\ll 1\%$  for the weaker, and likely more frequent standard of, GLEs. The exception here is GLE 42. We expect that we would have seen the increase in the HiSPARC data for GLE 42, but it pre-dates the HiSPARC project. We expect the same would have been true also for GLE 5, but we do not have the Kiel data to form the calibration, to predict the increase. GLE 5 was an exceptionally large event, for which we haven't seen anything similar in over half a decade. Such events are rare, and we expect that the energies involved would have shown a significant increase in the HiSPARC count rate.

These simulations, combined with the values given in Table 2.1, suggest that we would have expected an increase in the muon spectrum of no more than  $\sim 1\%$  (and more likely  $< 0.1\%$ ) for both GLE 71 and 72, which rules their observation with HiSPARC as extremely unlikely and may explain why we were unable to observe them in the earlier investigation. Therefore, from these results we must conclude that the HiSPARC network, in its current state, is unable to observe the ‘typical’, frequent standard GLEs, but it is likely able to observe the rare, highly energetic events, such as those seen in 1956 leading to GLE 5.

## 2.9 Conclusion

We have presented a feasibility study of using the existing HiSPARC network of muon detectors as a monitor of space weather events through calculating the observing properties of the stations, investigating the presence of signatures of space weather events in the existing data for five HiSPARC stations, both in its raw form and after performing corrections for atmospheric effects, and performing cosmic ray air shower simulations.

Using simulations of the interactions between CRs with the Earth’s magnetosphere in the PLANETOCOSMICS tool, we were able to calculate the rigidity cut-off and AVDs of the HiSPARC stations. We showed that the rigidity cut-off limits the

PCRs to particles with energies on the order of and above  $\sim 10^9$  eV. The AVDs were useful in demonstrating that lower rigidity PCRs that are observable are deflected significantly by the Earth's magnetosphere that we can observe solar eruptive events when the station is not in-line with the Sun.

In the raw HiSPARC data we found that we were unable to clearly detect signatures of the FDs or GLEs that have occurred over the lifetime of the HiSPARC network. It was observed that a major factor making it difficult to observe the space weather signatures was due to atmospheric effects causing additional variations in the data. Using a linear relationship between the logarithm of the normalised CR counts against both the zero-centred pressure and temperature, the atmospheric effects were removed from the data.

After the removal of the atmospheric effects, when investigation the correct HiSPARC data we found that we were still unable to observe any GLEs. The same was true for most of the FDs; however, we do speculate that we were able to observe a signature of a FD in December 2014.

A further study was conducted to understand the flux of muons at ground level, and in particular how the flux varies during GLEs. Using Monte Carlo simulations of particle transport through the atmosphere for given incident PCRs, were were able to interrogate the number and radial distribution of muons arriving at ground levels per PCR, which highlighted that the flux of muons is very low for PCRs with energies less than of in the region of the rigidity cut-off of the HiSPARC stations. This analysis therefore showed that any increase in the CR count from GLEs would likely be very low, due to the diffuse nature of the air showers induced by low-energy PCRs associated with causing GLEs

To expand on this analysis, a comparative study was conducted using the MAIRE tool. This allowed us to directly predict the increase in CR counts based on simulations of incident PCRs, and compare the output muon spectra from GCRs and GLEs. A calibration was necessary, to ensure that the MAIRE predictions were

consistent with the NMDB observations; however, upon applying this calibration, we were able to show that the predicted increase in the muon count rate was significantly lower than the neutron count rate, for each of the six GLEs studied. This led us to conclude that the HiSPARC network will be only capable of observing the most energetic GLEs, which occur less frequently than their lower energy equivalents.

We leave the reader with the following points:

1. The rigidity cut-off and AVDs of the HiSPARC stations were calculated using PCR transport simulations. We found the HiSPARC stations generally have a cut-off rigidity in the range,  $R_C \sim 3.0 - 3.5$  GV, setting a limit on the PCRs observable on the order of  $\sim 10^9$  GeV. The asymptotic viewing directions for the HiSPARC stations are close to equatorial for low rigidity PCRs, between  $\pm 20^\circ$  in latitude, and head towards the station's zenith for high rigidities.
2. Investigations of the raw and atmospheric corrected data showed no signatures of GLEs in the HiSPARC data. We propose that one FD was observed as a  $\sim 2\%$  decreased in the atmospheric-effects corrected data; however, none of the other FDs were observed in the HiSPARC data.
3. The CORSIKA air shower simulations showed that the flux of muons at ground level from lower energy GCRs is very low, with diffuse air shows induced. With the current configuration of the HiSPARC network, which strongly relies on the triggering of multiple detectors within a station, the observations are biased to higher energies, hence showing a limitation of the HiSPARC network for space weather observations.
4. The MAIRE simulations showed that for some of the largest GLEs to-date, we predicted the increase in the HiSPARC count rate to increase on average by no more than  $\sim 1\%$ , and only the most energetic events, with a low occurrence frequency would induce an increase in the HiSPARC count rate by  $> 5\%$ . This showed that the HiSPARC stations are therefore generally incompatible with

monitoring the lower limits of space weather activity, and only suitable as a monitor of the more extreme events.

This investigation has shown that the feasibility of using the HiSPARC network as a reliable tool for the monitoring of space weather is low; however, we have shown that for some specific cases, we expect to be able to make observations. One of the major issues with the HiSPARC network in its current configurations is the design of the stations. The triggering of multiple detectors biases the stations to observe higher energy PCRs. Since 2016, many HiSPARC stations have been sending the count rates of the individual detectors, the singles rates, which overcomes this biasing problem; however, this data is often inconsistent between stations and demonstrates a strong diurnal variation. The current method of removing the temperature-induced diurnal variation uses the atmospheric temperature, and not the temperature inside of the rooftop boxes, which we believe will have a stronger relationship and provide more accurate removal of the temperature variation in the data.

To overcome these effects, in the next chapter, we investigate the benefits of changing the configuration of a HiSPARC station, to determine whether we can improve the capabilities of the HiSPARC stations as a space weather monitoring network.

# Bibliography

- Augusto C., Navia C., de Oliveira M. N., Fauth A., Nepomuceno A., 2016, [Publ Astron Soc Jpn Nihon Tenmon Gakkai](#), 68
- Bartels R. T., 2012, Technical report, The HiSPARC Experiment: An Analysis of the MPV and the Number of Events per Unit Time. University College Utrecht
- Berkova M. D., Belov A. V., Eroshenko E. A., Yanke V. G., 2011, [Bull. Russ. Acad. Sci. Phys.](#), 75, 820
- Blackmore E. W., Stukel M., Trinczek M., Slayman C., Wen S., Wong R., 2015, [IEEE Transactions on Nuclear Science](#), 62, 2792
- Corti C., Potgieter M. S., Bindi V., Consolandi C., Light C., Palermo M., Popkow A., 2019, [ApJ](#), 871, 253
- Danilova O. A., Demina I. M., Ptitsyna N. G., Tyasto M. I., 2019, [Geomagnetism and Aeronomy](#), 59, 147
- Desorgher L., 2005, Technical Report PLANETOCOSMICS-SUM, PLANETOCOSMICS Software User Manual, <http://cosray.unibe.ch/~laurent/planetocosmics/>. University of Bern, <http://cosray.unibe.ch/~laurent/planetocosmics/>
- Desorgher L., Flckiger E. O., Gurtner M., 2006. p. 2361, <http://adsabs.harvard.edu/abs/2006cosp...36.2361D>
- Dorman L. I., 1972, Kosm. Luchi, no. 13, pp. 5-66
- Dubey A., Kumar S., Dubey S. K., 2016, [Journal of Physics: Conference Series](#), 755, 012056
- Dyer C. S., Lei F., Clucas S. N., Smart D. F., Shea M. A., 2003, [Advances in Space Research](#), 32, 81
- ETEnterprises 2020, Technical Report 9125B, Data Sheet: 9125B Series, <http://et-enterprises.com/products/photomultipliers/product/p9125b-series>. ET Enterprises, <http://et-enterprises.com/products/photomultipliers/product/p9125b-series>
- Fokkema D. B. R. A., 2012, PhD thesis, University of Twente
- Fokkema D. B. R. A., de Laat A. P. L. S., Kooij T., 2012, SAPPHIRE, <https://github.com/HiSPARC/sapphire>

- Heck D., Pierog T., 2017, Technical Report 7.6400, Extensive Air Shower Simulation with CORSIKA: A Users Guide
- Herbst K., Kopp A., Heber B., 2013, *Annales Geophysicae*, 31, 1637
- Lei F., Clucas S., Dyer C., Truscott P., 2004, *IEEE Transactions on Nuclear Science*, 51, 3442
- Lingri D., Mavromichalaki H., Belov A., Eroshenko E., Yanke V., Abunin A., Abunina M., 2016, arXiv:1612.08900 [astro-ph]
- McCracken K. G., Moraal H., Shea M. A., 2012, *ApJ*, 761, 101
- Mendonça R. R. S. d., et al., 2016, *ApJ*, 830, 88
- Mishra R. K., Mishra R. A., 2007, *Pramana*, 68, 407
- Mishra R. K., Mishra R. A., 2008, Rom. Journ. Phys., 53, 925
- NMDB 2018, NMDB Event Search Tool (NEST), <http://www.nmdb.eu/nest/>
- Paschalis P., Mavromichalaki H., Yanke V., Belov A., Eroshenko E., Gerontidou M., Koutroumpi I., 2013, *New Astronomy*, 19, 10
- Pereira E. G., Vasconcellos C. A. Z., Hadjimichel D., 2020, arXiv:2011.06480 [hep-ex, physics:hep-ph]
- Savi M., Maleti D., Jokovi D., Veselinovi N., Banjanac R., Udovii V., Dragi A., 2015, *J. Phys.: Conf. Ser.*, 632, 012059
- Shea M. A., Smart D. F., McCracken K. G., 1965, *J. Geophys. Res.*, 70, 4117
- Thomas S., Owens M., Lockwood M., Owen C., 2017, *Ann. Geophys.*, 35, 825
- van Dam K., van Eijk B., Fokkema D. B. R. A., van Holten J. W., de Laat A. P. L. S., Schultheiss N. G., Steijger J. J. M., Verkooijen J. C., 2020, *Nuclear Instruments and Methods in Physics Research Section A: Accelerators, Spectrometers, Detectors and Associated Equipment*, 959, 163577